Ages and tectonic implications of the mafic–ultramafic–carbonatite intrusive rocks and associate Cu–Ni, Fe–P and apatite–vermiculite deposits from the Quruqtagh district, NW China

Article *in* Ore Geology Reviews · July 2016

DOI: 10.1016/j.oregeorev.2016.07.011

CITATIONS
2

READS
111

9 authors, including:

Chunming Han
Chinese Academy of Sciences
86 PUBLICATIONS **4,643** CITATIONS
SEE PROFILE

Wenjiao Xiao
Chinese Academy of Sciences
479 PUBLICATIONS **19,354** CITATIONS
SEE PROFILE

Benxun Su
Chinese Academy of Sciences
150 PUBLICATIONS **2,527** CITATIONS
SEE PROFILE

Patrick Asamoah Sakyi
University of Ghana
83 PUBLICATIONS **1,258** CITATIONS
SEE PROFILE

Ore Geology Reviews xxx (2016) xxx–xxx

Contents lists available at ScienceDirect

Ore Geology Reviews

journal homepage: www.elsevier.com/locate/oregeorev

Ages and tectonic implications of the mafic–ultramafic-carbonatite intrusive rocks and associated Cu-Ni, Fe-P and apatite-vermiculite deposits from the Quruqtagh district, NW China

Chunming Han [a,b,*], Wenjiao Xiao [a,b], Benxun Su [a], Patrick Asamoah Sakyi [c], Songjian Ao [a], Jien Zhang [a], Bo Wan [a,b], Dongfang Song [a], Zhongmei Wang [a]

[a] Key Laboratory of Mineral Resource, Institute of Geology and Geophysics, Chinese Academy of Sciences, Beijing 100029, China
[b] CAS Center for Excellence in Tibetan Plateau Earth Sciences, Beijing 100101, China
[c] Department of Earth Science, University of Ghana, P.O. Box LG 58, Legon-Accra, Ghana

ARTICLE INFO

Article history:
Received 9 September 2015
Received in revised form 14 July 2016
Accepted 18 July 2016
Available online xxxx

Keywords:
SIMS zircon U-Pb
Ultramafic–mafic-carbonatite
Quruqtagh, Tarim Craton, NW China

ABSTRACT

The Tarim Craton is an important tectonic unit and a suitable target to investigate and understand the Proterozoic tectonic framework of the Central Asian Orogenic Belt and supercontinent Rodinia. Precambrian ultramafic–mafic-carbonatite rocks are widely distributed in the Quruqtagh domain of NE-Tarim. In the Quruqtagh, Cu-Ni, Fe-P and apatite-vermiculite deposits hosted in the ultramafic-mafic-carbonatite rocks occur in the Xingdi, Qieganbulake, Daxigou, and Kawuliuke. These deposits associated with the ultramafic-mafic-carbonatite rocks in Quruqtagh formed in a period between the Paleoproterozoic and Neoproterozoic. The Paleoproterozoic Fe-P deposit is represented by the Daxigou deposit that yielded a SIMS U-Pb zircon age of 2452 ± 10 Ma. The other Cu-Ni, Fe-P and apatite-vermiculite deposits, hosted in the ultramafic–mafic rocks, formed in the Neoproterozoic, represented by the Xingdi, Kawuliuke, and Qieganbulake deposits that formed between 812 Ma and 707 Ma. The Paleoproterozoic mineralization event was coincident with the global collisional events that led to the assembly of the Paleo-Mesoproterozoic Columbia (Nuna) supercontinent. And the emplacement of these Neoproterozoic ultramafic-mafic-carbonatite rocks was related to a mantle plume event that led to the breakup of the Tarim Craton from the Rodinia supercontinent.

1. Introduction

There are three large cratons in China, namely; the Tarim, North China and Yangtze cratons, which were amalgamated during Phanerozoic orogenic processes. The Tarim Craton is situated in the Xinjiang Uygur Autonomous Region of northwestern China, and covers an area of 530,000 km^2. Its central part is occupied by a desert, and outcrops are only present along its margins. The craton looks like a huge eyeball and is surrounded by the Tianshan Mountain (orogen) to the north, the western and the Central-Southern Altyn Tagh Mountain (orogen) to the southeast (Fig. 1).

During the past fifty years many geological and ore-deposit investigations have led to the discovery of many skarn Cu–Mo (e.g. Dapingliang), porphyry Cu-Au (Qiongtage), mafic–ultramafic mineral deposits (Xingdi Cu–Ni deposit, Kawuliuke and Daxigou Fe-P deposits), and the Qieganbulake apatite-vermiculite deposit (Chen, 1989; Feng et al., 1995; Li et al., 1998; Huang et al., 2002; Yuan et al., 2002; Sun and Huang, 2007; Xia et al., 2009; Cao et al., 2011; Xia et al., 2011, 2012). However, most of the documentation of these deposits has been reported in the Chinese literature, for which reason the international geological community knows little about these deposits until now.

Although several investigations have been carried out on the Quruqtagh magmatic suites (Zhu et al., 2008; Cao et al., 2011; Long et al., 2011, 2012; Zhang et al., 2012a, 2012b), there is no consensus yet regarding the geodynamic mechanism by which such voluminous and diverse magmas were generated. Models proposed to explain the driving force for magmatism include: (1) the Tarim Craton was possibly located on the periphery of the proposed Rodinian superplume (Li et al., 2003a, 2003b), but little has been known about the Neoproterozoic igneous rocks in the Tarim Craton in response to this superplume activity; (2) Precambrian mafic-ultramafic intrusions have been regarded as magmatism related to the ca. 1000–800 Ma Jinin orogeny (Xinjiang BGMR, 1993; Feng et al., 1995; Jiang et al., 2005); (3) during the Neoproterozoic, multiple epidodes (at least three pulses) of rifting occurred within the Tarim Craton (Zhu et al., 2008). Precise geochronology and systematic geochemical data are rare for these rocks.

* Corresponding author at: Key Laboratory of Mineral Resource, Institute of Geology and Geophysics, Chinese Academy of Sciences, Beijing 100029, China.
E-mail address: cm-han@mail.iggcas.ac.cn (C. Han).

http://dx.doi.org/10.1016/j.oregeorev.2016.07.011
0169-1368/

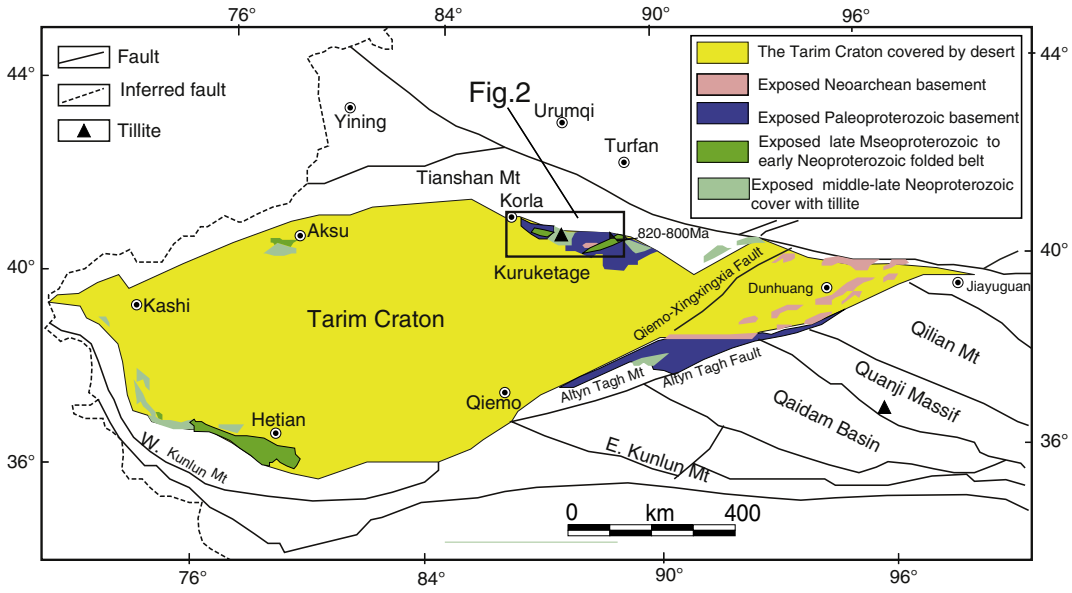

Fig. 1. Simplified geological map of the Tarim Craton surrounding areas, bordered by major structures (after Lu et al., 2008).

In this paper, we present a comprehensive geochronological and geochemical analysis of the mafic-ultramafic complex associated with the carbonatite in the Quruqtagh region of the northeastern Tarim Craton, with the aim of characterizing their petrogenesis and constraining their genesis and geodynamic context. Our study has important implications for Cu-Ni exploration potential of other mafic-ultramafic-carbonatite bodies in the region, indeed, through much of the Central Asian Orogenic Belt (CAOB, Windley et al., 2007; Xiao et al., 2015).

2. Geological setting

The Tarim Craton records Precambrian evolutionary history of NW China and its adjacent areas (Lu et al., 2008; Zhao and Peter, 2012).

The Tarim Craton covers an area of 530,000 km^2. The EW-trending Quruqtagh uplift with a width of 50–70 km is located in the NE margin of the Tarim Craton. The voluminous Neoproterozoic slightly metamorphosed rocks (slate-phyllite, meta-igneous rocks) and various Mesoproterozoic, locally Paleoproterozoic-Archean schists, gneisses and amphibolites exposed in Quruqtagh, which forms the ancient basement of the Tarim Craton (Gao et al., 1993; Lu et al., 2008). Four diamictite intervals related to Neoproterozoic glaciations are well preserved (Xu et al., 2003, 2005; Xiao et al., 2004). A Neoproterozoic continental rift environment is evidenced by various 830–740 Ma magmatic rocks in the northern Tarim Craton, as a consequence of the break-up of Rodinia (Huang et al., 2005; Zhang et al., 2007, 2011, 2012a, 2012b).

The Neoproterozoic rocks occur in Xishankou, Xinger and Saimashan areas along the northeastern margin of the Tarim Craton. Correlation based on similar lithology between them has been proposed (Gao and Zhu, 1984; Gao and Qian, 1985). These rocks unconformably overlie the Mesoproterozoic Paergangtage Group and are unconformably overlain by the lower Cambrian siliceous rocks. The Neoproterozoic succession is divided into the upper and lower parts, and each is composed of four formations. The lower part comprises the Beiyixi, Zhaobishan, Altungal, and Tereeken formations, and the upper part, is made up of the Zhamoketi,Yukengou, Shuiquan and Hangelchaok formations. The thickest and most complete Neoproterozoic sections consisting of all eight formations occur in the Xinger, Saimashan and Xishankou areas. The Neoproterozoic rocks in the northeastern Tarim Craton are characterized by several horizons of glacier deposits and volcanic rocks, separated by thick layers of shale, sandstone and limestone. The glacier deposits have been recognized from the Beiyixi, Altungal, Tereeken and Hangelchaok formations and three glaciations, namely; Beiyixi, Tereeken and Hangelchaok, have been reported (Wang et al., 1981; Gao and Zhu, 1984; Gao and Qian, 1985; Gao and Qian, 1985; Brookfield, 1994; Knoll, 2000; Xu et al., 2003; Xiao et al., 2004). Besides these four diamictite-bearing formations, interglacial deposits are found to contain interbedded sandstones and shales of the Zhaobishan and Zhamoketi formations, carbonates of the Shuiquan Formation and shales of the Yukengou Formation. The Neoproterozoic volcanic rocks occur in the Beiyixi, Altungal, Zhamoketi and Shuiquan formations. The volcanic rocks in the Altungal and Shuiquan formations comprise several intercalated thin layers (0.3–3 m) of basalts or trachybasalts; whereas the volcanic rocks in the Zhamoketi Formation are composed of much thicker (up to ~250 m) dacites and andesitic porphyrites (Gao and Qian, 1985).

Three regional-scale faults occur in the Quruqtagh domain. The Korla-Xingdi fault is characterized by the north-directed thrust slices of the Proterozoic schist-gneiss and the Paleozoic limestone onto the Jurassic coal-bearing rocks in the Hejing basin, suggesting its Cenozoic activity. The Kumux-Hejing fault is considered as a Late Paleozoic boundary between central and southern Tianshan, along or near which the north-verging ophiolitic mélanges and granulite lens occur, indicating late Paleozoic sutures (Gao et al., 1995; Shu et al., 2004). The Xingdi fault is an important boundary between the Quruqtagh uplift and the Tarim Craton (Shu et al., 2004; Fig. 2).

Previous researches have tentatively concluded a four-stage tectonic evolution documented in the rocks of the Xingdi fault zone (Gao et al., 1993; Deng et al., 2008; Zhu et al., 2008). The first stage took place in pre-Nanhua Period (before ca. 800 Ma) and was characterized by strong folding, ductile shearing and magmatism dated at an interval of 900–1100 Ma (Shu et al., 2011). The second stage recorded voluminous bimodal magmatism and basic dyke swarm dated at 830–740 Ma (Zhu et al., 2008), revealing that multiple episodes of rifting took place within the Tarim Craton, which formed two contrasting sedimentary areas on two sides of the Xingdi fault. The third stage was marked by Permian conglomerates unconformably overlying Carboniferous sandy-muddy rocks. Recent work has provided evidence for post-orogenic crustal melting dated at 270–290 Ma by magmatic zircons from granitic plutons (Zhu, 2007). The fourth stage occurred during the Neogene and was marked by a north-verging thrust, followed by a dextral strike-slip shear (Shu et al., 2011; Fig. 2).

Please cite this article as: Han, C., et al., Ages and tectonic implications of the mafic–ultramafic-carbonatite intrusive rocks and associated Cu-Ni, Fe-P and apatite-vermic..., Ore Geol. Rev. (2016), http://dx.doi.org/10.1016/j.oregeorev.2016.07.011

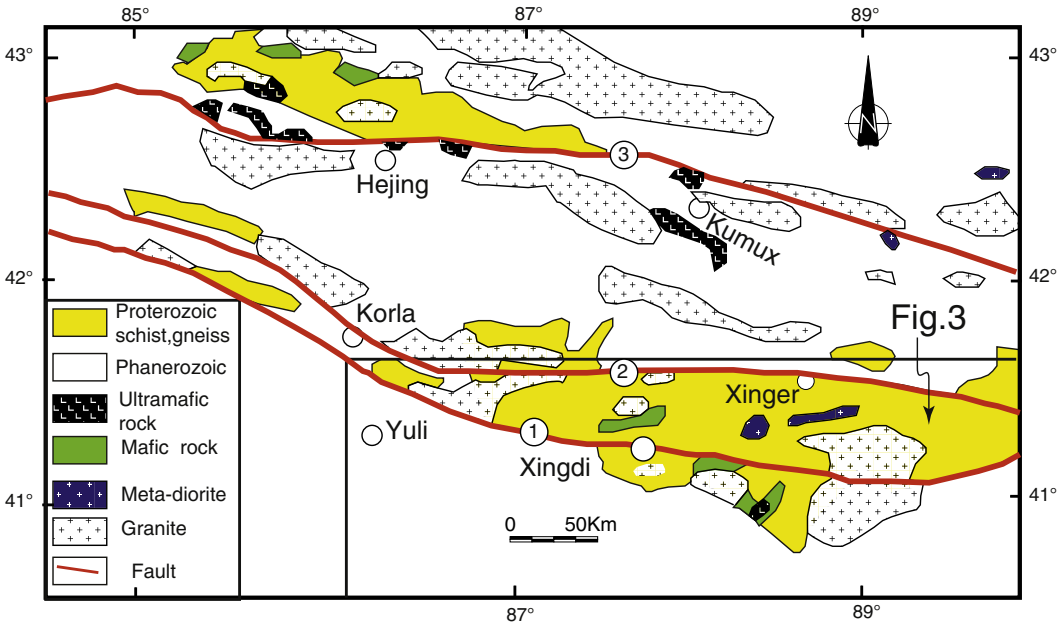

Fig. 2. Regional geological map of the Quruqtagh domain in NE-Tarim (after Shu et al., 2011). (1) the Xingdi fault forming the southern boundary of the Quruqtagh domain; (2) the Korla-Xinger forming the northern boundary of the Quruqtagh domain; (3) the Kumux-Hejing fault between the Paleozoic central Tianshan and southern Tianshan belts.

3. Geology of mineral deposits

The Quruqtagh area is situated in the northeastern Tarim Craton, northwestern China. The Neoproterozoic igneous rocks in this area, including mafic-ultramafic-(carbonatite) complexes (Huang, 2001; Huang et al., 2002; Zhang et al., 2007), mafic dykes, and granitoids (Feng et al., 1995; Hu et al., 2000; Lu and Yuan, 2003) (Fig. 2), were generally thought to have been formed during the Jinning orogeny (ca. 1000–800 Ma) which resulted in the final crystallization of the regional Precambrian basement of the Tarim Craton (Feng et al., 1995; Jiang et al., 2005). Consistent with the Jinning orogenic model, some of the mafic-ultramafic intrusions at the southern Quruqtagh region have been interpreted as Neoproterozoic ophiolites or late Mesoproterozoic rift-related intrusive complexes (Guo et al., 2005; Fig. 3). There are five main mafic-ultramafic-(carbonatite) intrusions along the southern margin of the Quruqtagh region. They are distributed approximately in E-W direction (Fig. 3). These mafic-ultramafic-carbonatite complexes, in the northeastern margin of the Tarim can be considered prospective for Ni-Cu, Fe–P and apatite-vermiculite deposits mineralization.

The major deposits associated with mafic-ultramafic-carbonatite complexes in Quruqtagh are represented by the Xingdi, Qieganbulake, Daxigou and Kawuliuke deposits (Fig. 3).

3.1. Xingdi Cu-Ni deposit.

The Xingdi Cu-Ni deposit exhibits a funnel-shaped cross-section according to field and drill-hole data (Yuan et al., 2002; Fig. 4). It intrudes the Paleoproterozoic Xingditage Group amphibolite facies metasedimentary rocks, consisting of an early ultramafic unit (Unit I), a younger layered mafic-ultramafic-intermediate unit (Unit II), and a late mafic unit (Unit III). The contacts between different petrographic phases are sharp but no chilled margin has been observed.

Unit I comprises about 5% of the outcrop area of the complex, and according to field mapping and drilling results, it appears to be rootlessly

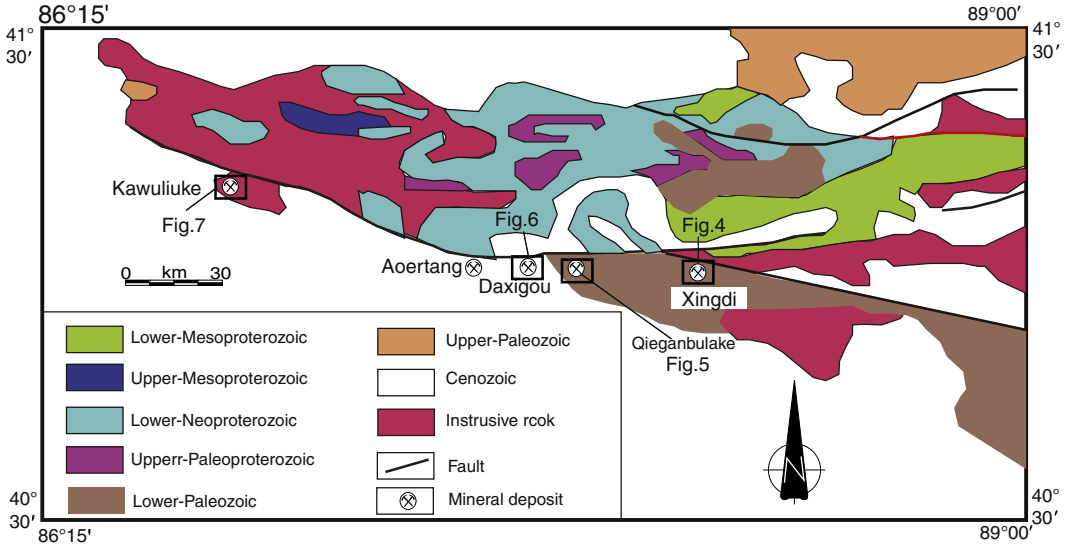

Fig. 3. Simplified geological map of the Eastern Quruqtagh domain, showing the main Cu-Ni, Fe-P and apatite-vermiculite deposits (after Xia et al., 2012).

Please cite this article as: Han, C., et al., Ages and tectonic implications of the mafic–ultramafic-carbonatite intrusive rocks and associated Cu-Ni, Fe-P and apatite-vermic..., Ore Geol. Rev. (2016), http://dx.doi.org/10.1016/j.oregeorev.2016.07.011

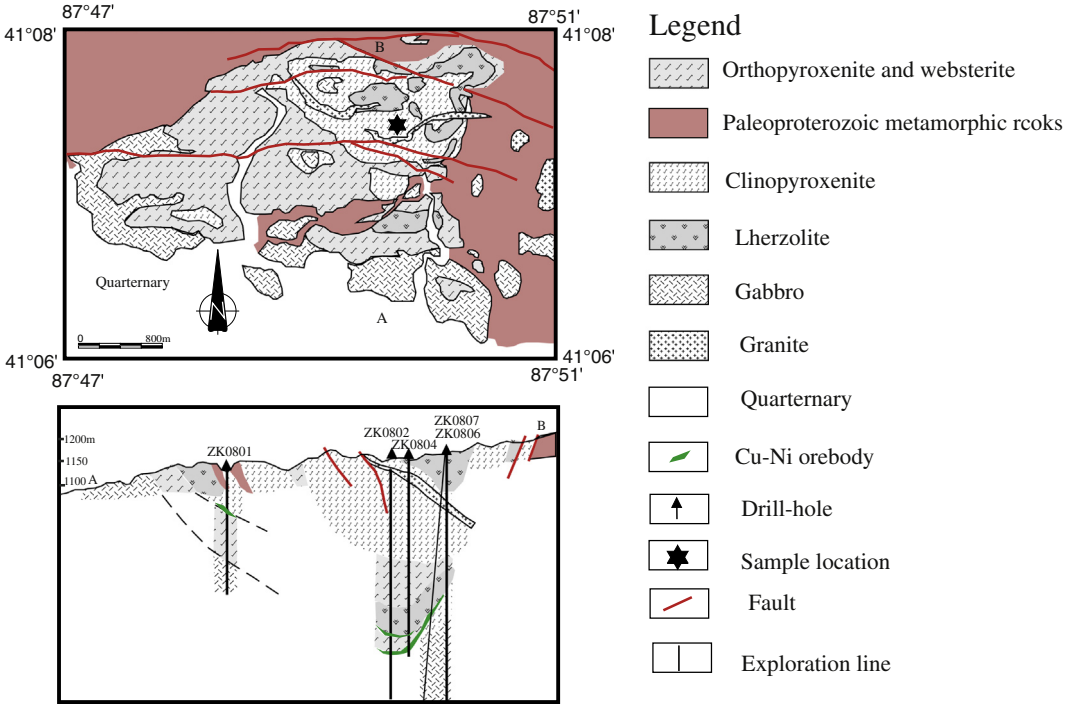

Fig. 4. Simplified geological map of Xingdi Cu-Ni deposit (after Yuan et al., 2002).

suspended in the pyroxenite and gabbro (Unit II). It is emerald-green in colour, exhibits medium to coarse granular texture, and consists of relatively homogeneous lherzolite containing olivine (50–70%) with variable amounts of clinopyroxene (5–15%), orthopyroxene (25–35%), and minor magnetite (1–5%), plagioclase (<1–2%), phlogopite (<1%), chromite (<1%) and sulphide (<1.0%). Olivine is normally rounded and occasionally enclosed by orthopyroxene or clinopyroxene oikocrysts. The phlogopite is likely a primary mineral phase as shown by its relatively euhedral crystal form. Locally, slight serpentinization is visible around the grain margins of olivine.

Unit II makes up about 70% of the outcrop area of the complex and in a bottom-up succession, it consists of pyroxenite, gabbro, and diorite. The pyroxenite could be subdivided into several zones based on the relative proportion of orthopyroxene to clinopyroxene, namely; orthopyroxenite, websterite, and clinopyroxenite zones. Gabbros in this unit include orthopyroxene-, olivine- gabbro, and clinopyroxene-bearing gabbro. The diorites are the most fractionated member of this unit and occur as small rootless stocks suspended on the topmost parts of the gabbro unit, indicating that they are fractionated products of the evolved gabbroic magma. The diorites contain 10–15% quartz, 35–50% hornblende, 35–45% plagioclase and minor clinopyroxene (2–5%) occasionally enclosed in hornblende or plagioclase oikocrysts. Accessory minerals are apatite, titanite and zircon. Layered structure in this unit, exhibiting varying contents of mafic minerals and plagioclase, which indicate that most of the rocks crystallized in situ.

Unit III is a gabbro unit and accounts for about 25% of the complex. The unit include noritic gabbro, websteritic gabbro, clinopyroxene gabbro and (olivine-bearing) gabbro. They are of medium to coarse grain structure and contain varying percentages of clinopyroxene (30–55%), orthopyroxene (10–40%), plagioclase (30–60%), minor quartz (<1%) or olivine, and accessory minerals like apatite, zircon and Ti-Fe oxides.

Exploration work indicates that the Xingdi contains 20,339 t of Cu + Ni (Yuan et al., 2002), with ore grades of 0.2–0.8 wt.% Cu, 0.1–0.6 wt.% Ni, and 0.01–0.05 wt.% Co (Li et al., 1998). The ore bodies generally occur at the boundaries between lherzolite and orthopyroxenite or between pyroxenite and gabbro. Main ore type is sparsely disseminated sulfides (5–10% sulfides), occurring as fine interstitial to cumulus minerals.

3.2. Qieganbulake apatite-vermiculite deposit

The Qieganbulake complex is intruded into Palaeoproterozoic gneisses and amphibolites (Fig. 5). It occurs as an elliptical, concentrically zoned structure elongated within a NWW–SEE fracture (Fig. 5), with a total exposed area of 1.5 km^2. The complex is composed mainly dunite, carbonatite, phlogopitelite, and pyroxenite. The carbonatites form discontinuous outcrops such as sporadic dykes and veins along the fractures that traverse the Qieganbulake complex with maximum exposure in the eastern part of the complex. The outermost ring of the complex is apatite-bearing pyroxenites rimming phlogopitelites.

Dunite accounts for ~3% of the complex, and is strongly serpentinized. The dunites are mainly present as angular or rounded xenoliths in all rock types, especially in the center of the complex. The curved and crenellate borders in the rocks suggest that they were in a molten state during emplacement.

The carbonatites account for ~15% of the complex and are dominated by calciocarbonatites (Chen, 1989; Yin, 1992; Huang, 2001; Zhang et al., 2007). The carbonatites have a typical coarse-grained granular texture, consisting of calcite and dolomite with subordinate amounts of apatite, phlogopite, magnetite, and ilmenite. Accessory minerals include baddeleyite, calzirtite, pyrochlore, and monazite. Calcite grains show banded structures with Fe-Ti oxide minerals and apatite clusters (Chen, 1989; Huang, 2001).

The phlogopitelite, accounting for ~25% of the complex, consists almost entirely of phlogopite, ranging from 0.5 mm to 3 cm in size. Diopside and Ti-magnetite are present as accessory mineral phases. The pyroxenites constitute ~60% of the complex, and are composed of diopside, phlogopite and apatite, displaying typical cumulate texture. Accessory minerals include magnetite, titanite, and zircon. Apatite is commonly present as granular segregations, or as parallel and radiating columnar aggregates filling fractures (Chen, 1989; Huang, 2001; Ye et al., 2013).

Please cite this article as: Han, C., et al., Ages and tectonic implications of the mafic–ultramafic-carbonatite intrusive rocks and associated Cu-Ni, Fe-P and apatite-vermic..., Ore Geol. Rev. (2016), http://dx.doi.org/10.1016/j.oregeorev.2016.07.011

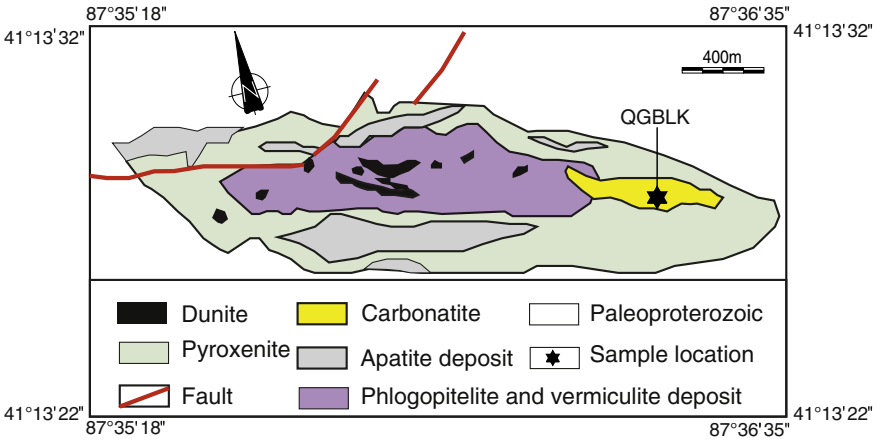

Fig. 5. Simplified geological map of Qieganbulake apatite-vermiculite deposit (after Ye et al., 2013).

3.3. Daxigou Fe-P deposit.

The Daxigou Complex hosts Fe-P deposit. The deposit is situated in the south of the Xingdi Fault with an area of 2.1 × 0.9 km (Fig. 6). The Daxigou Complex is made up mainly by greyish white anorthosite that exhibits coarse-grained granitic texture and blocky structure. The main mineral components are plagioclase (45–50%), quartz (25–30%), K-feldspar (14–17%), hornblende (8%), magnetite (1–2%) and apatite (1%). Accessory minerals include zircon and ilmenite. Syenogranites (SG) occur mainly as dykes accompanying the granodiorite, and account for 30% of the complex. Typically they are pinkish and show massive, medium- to coarse-grained granitic textures. Modal compositions include plagioclase (An 35–50%), quartz (25–35%), K-feldspar (18–22%), biotite (2–5%), hornblende (1–2%), and accessory minerals such as apatite, zircon and ilmenite (Xia et al., 2009, 2011, 2012). It has reserves of about 128 × 10^4 t of P_2O_5 and 11.29 × 10^4 t Fe, with P_2O_5 and TFe mean grades of 2.53–6.83%, and 14.15–20.92% respectively (Xia et al., 2012).

3.4. Kawuliuke Fe-P deposit.

The Kawuliuke deposit is located west of the Daxigou desposit and is 2000 m long and 950 m wide (Fig. 7). The Kawuliuke complex consists of pyroxenite, hornblende pyroxenite, hornblendite, hornblende gabbro and gabbro. Pyroxenite unit is grey to grey-green in colour and consists of diopside (65–85%), biotite, hornblende, magnetite and apatite. The hornblendite unit is grey-green in colour and consists mainly of 80% hornblende, and minor pyroxene, magnetite and apatite; the hornblende gabbro and gabbro units are grey to grey-green in colour and consists of 30–40% pyroxene, 40–50% plagioclase and minor hornblende, biotite, augite. Magnetite and apatite; Fe-P mineralization is present in the pyroxenite unit; The ore bodies are 400–1000 m long, 400–800 m width and with a thickness of 4–43 m. Three ore types, namely; massive, disseminated and taxitic structure ore, are recognized. The deposit contains 6752 × 10^4 t Fe and 131.47 × 10^4 t P_2O_5, with TFe and P_2O_5 mean grades of 14.77–28.68% and 2.25–9.26%, respectively (Xia et al., 2009, 2011, 2012).

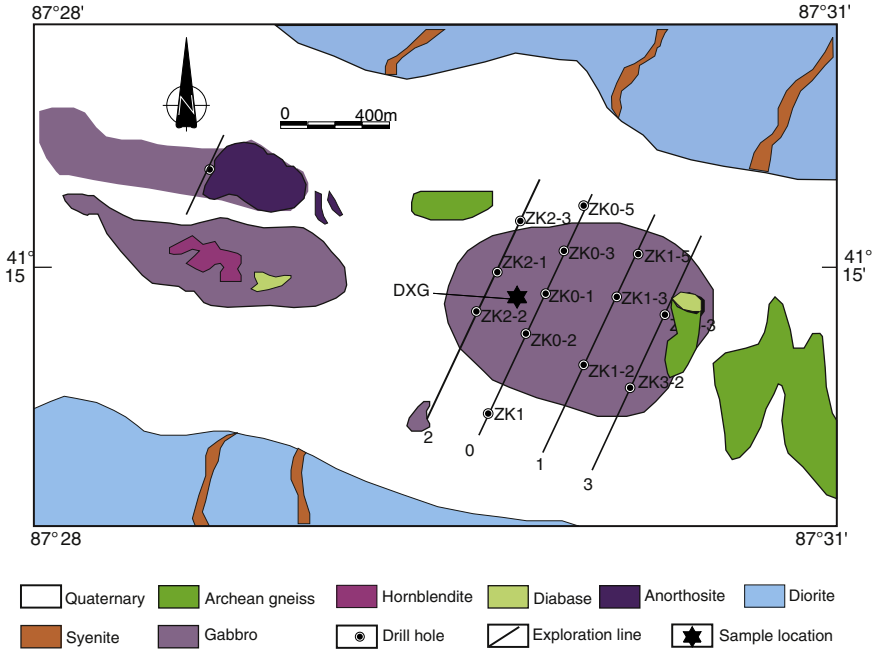

Fig. 6. Simplified geological map of Daxigou Fe-P deposit (after Xia et al., 2012).

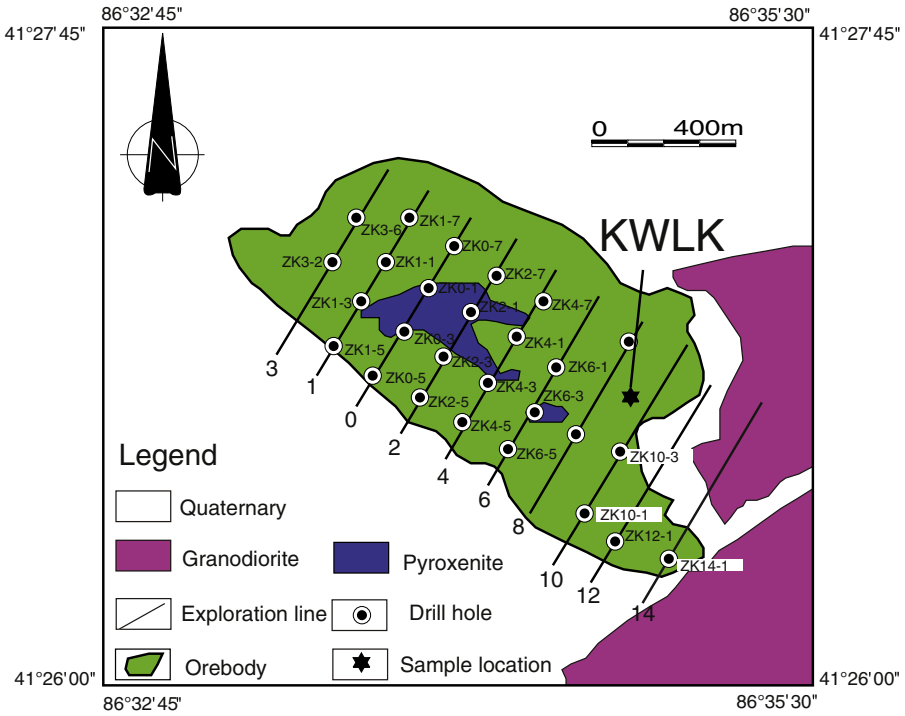

Fig. 7. Simplified geological map of Kawuliuke-P deposit (after Xia et al., 2012).

4. Analytical methods

Zircons were separated using conventional heavy liquid and magnetic techniques and picked under a binocular microscope. The grains were mounted along with Temora standard and then cast in epoxy resin in a 2.5 cm diameter mount and ground to expose the center of the grains. Internal structures of zircon were examined using cathodoluminescence (CL) images prior to U–Pb analyses. In-situ zircon U–Pb ages were acquired on the Cameca IMS-1280 ion microprobe (SIMS) in a single collector mode at the Institute of Geology and Geophysics (IGG), Chinese Academy of Sciences, Beijing. The U–Th–Pb ratios and absolute abundances were determined relative to the standard zircon 91,500 (Wiedenbeck et al., 1995), analyses of which were interspersed with those of unknown grains, using operating and data processing procedures similar to those described by Li et al. (2009a). The mass resolution used to measure Pb/Pb and Pb/U isotopic ratios was 5400 during the analyses. A long-term uncertainty of 1.5% (1 RSD) for $^{206}Pb/^{238}U$ measurements of the standard zircons was propagated to the unknowns (Li et al., 2009b), despite that the measured $^{206}Pb/^{238}U$ error in a specific session is generally around 1% (1RSD) or less. Measured compositions were corrected for common Pb using non-radiogenic ^{204}Pb. Corrections are sufficiently small to be insensitive to the choice of common Pb composition, and an average of present-day crustal composition (Stacey and Kramers, 1975) was used assuming that the common Pb is largely surface contamination introduced during sample preparation. Uncertainties on individual analyses are reported at a 1σ level; mean ages for pooled U/Pb (and Pb/Pb) analyses are quoted with 95% confidence interval. Data reduction was carried out using the Isoplot/Ex v. 2.49 program (Ludwig, 2001).

Five-kilogram samples for geochemical analyses were crushed using a ceramic jaw crusher; the resulting small chips were washed with distilled water and then powdered in an agate mortar. Major oxides were determined by X-ray Fluorescence (XRF) technique on fused glass beads using a Shimadzu XRF1500 sequential spectrometer at IGG. The analytical uncertainties are better than 5% as revealed by long-term measurements of Chinese national standards GSR-1 and GSR-3.

Trace-element abundances were measured by Inductively Coupled Plasma Mass Spectrometry (ICP-MS) using a Finnigan MAT Element spectrometer at IGG. About 50 mg of crushed whole-rock powder was dissolved using HF/HNO_3 (10:1) mixture in screw-top Teflon beakers for 7 days at ~100 °C, followed by evaporation to dryness, refluxing in 7 N HNO3 to incipient dryness again, and the sample cake was then re-dissolved in 2% HNO_3 to a sample/solution weight ratio of 1: 1000. An internal standard was used for monitoring drift in mass response during mass spectrometric measurements. Further details can be found in Gao et al. (2002).

5. Results

5.1. Zircon U-Pb geochronology

Four samples for U-Pb dating were selected from the Xingdi (XD, 87° 51′18″E, 41°07′30″N), Qieganbulake (QGBLK, 87°36′22″E, 41°13′27″N,), Daxigou (DXG, 87°29′46″E, 41°14′58″N) and Kawuliuke (KWLK, 86°34′ 03″E, 41°26′31.5″N) intrusions. These samples exhibit intergranular texture, consisting of equivalent grains of clinopyroxene and plagioclase with minor olivine and hornblende. Clinopyroxene and plagioclase are present in roughly sub-equal amounts and together account for some 80 to 85% of the rock. Zircon U-Pb age data for the gabbro samples are listed in Table 1 and shown in the concordia diagrams. We consider each of the obtained ages to represent the best estimate of the crystallization age of the host gabbro, and, consequently, of the formation of the respective deposits.

5.1.1. Xingdi intrusion

Zircons in this intrusion are mostly small, euhedral and colorless. In CL images (Fig. 8), no inherited cores were observed. They have high U (195–1175 ppm) and Th (66–913 ppm) contents, and high Th/U ratios (0.25–0.84) (Table 1). Such features indicate that they crystallized from magmas (Wu et al., 2006). Twelve analyses of 22 zircon grains (Table 1) form a tight cluster on concordia and yielded a weighted mean $^{206}Pb/^{238}U$ age of 737 ± 2 Ma (1σ, MSWD = 0.038, Fig. 9).

Please cite this article as: Han, C., et al., Ages and tectonic implications of the mafic–ultramafic-carbonatite intrusive rocks and associated Cu-Ni, Fe-P and apatite-vermic..., Ore Geol. Rev. (2016), http://dx.doi.org/10.1016/j.oregeorev.2016.07.011

Table 1
SIMS U-Pb data for zircons from gabbros in the Quruqtagh, Xinjiang.

Sample spot	U (ppm)	Th (ppm)	$\frac{Th}{U}$	f_{206}[a] (%)	$\frac{^{207}Pb}{^{206}Pb}$	±1σ (%)	$\frac{^{207}Pb}{^{235}Pb}$	±1σ (%)	$\frac{^{206}Pb}{^{238}Pb}$	±1σ (%)	$t_{207/235}$ (Ma)	±1σ	$t_{206/238}$ (Ma)	±1σ
Xingdi II Cu-Ni deposit(GPS coordinate: 41°07′30″N, 87°51′18″E)														
XD-1	195	66	0.34	0.09	0.0635	1.15	1.0634	1.89	0.1214	1.50	735.5	9.9	738.4	10.5
XD-2	513	130	0.25	0.28	0.0637	1.02	1.0463	1.99	0.1192	1.71	727.1	10.4	725.9	11.7
XD-3	141	90	0.64	0.01	0.0640	1.15	1.0762	1.90	0.1219	1.52	741.8	10.1	741.5	10.7
XD-4	221	146	0.66	0.04	0.0649	0.92	1.0744	1.76	0.1200	1.51	740.9	9.3	730.6	10.4
XD-5	492	407	0.83	0.02	0.0636	0.62	1.0823	1.70	0.1235	1.59	744.7	9.0	750.4	11.3
XD-6	293	171	0.58	0.02	0.0642	0.79	1.0764	1.70	0.1216	1.51	741.9	9.0	739.9	10.5
XD-7	681	551	0.81	0.02	0.0646	0.53	1.0881	1.59	0.1222	1.50	747.6	8.5	742.9	10.6
XD-8	354	261	0.74	0.04	0.0636	0.75	1.0808	1.68	0.1232	1.50	744.0	8.9	749.1	10.6
XD-9	308	222	0.72	0.05	0.0639	1.15	1.0466	1.89	0.1189	1.50	727.2	9.9	724.1	10.3
XD-10	640	413	0.65	0.04	0.0637	0.87	1.0664	1.74	0.1214	1.51	737.0	9.2	738.9	10.5
XD-11	370	277	0.75	0.04	0.0635	0.87	1.0755	1.74	0.1228	1.51	741.4	9.2	746.4	10.6
XD-12	602	177	0.29	0.06	0.0637	0.58	1.0720	1.64	0.1221	1.53	739.7	8.6	742.5	10.7
XD-13	377	153	0.41	0.02	0.0638	0.83	1.0500	1.77	0.1194	1.56	728.9	9.2	727.3	10.7
XD-14	1175	913	0.78	0.02	0.0640	0.55	1.0737	1.64	0.1217	1.54	740.5	8.6	740.5	10.8
XD-15	398	287	0.72	0.02	0.0644	0.93	1.0756	1.82	0.1212	1.56	741.5	9.6	737.5	10.9
XD-16	342	251	0.73	0.03	0.0640	0.74	1.0362	1.67	0.1175	1.50	722.0	8.7	716.0	10.2
XD-17	344	290	0.84	0.02	0.0632	1.16	1.0662	1.90	0.1223	1.50	736.9	10.0	743.7	10.5
XD-18	500	399	0.80	0.03	0.0639	0.69	1.0716	1.70	0.1215	1.55	739.5	9.0	739.5	10.8
XD-19	497	323	0.65	0.02	0.0635	0.60	1.0518	1.63	0.1202	1.52	729.8	8.5	731.8	10.5
XD-20	397	299	0.75	0.02	0.0637	0.66	1.0657	1.64	0.1213	1.50	736.6	8.6	737.9	10.5
XD-21	377	263	0.70	0.03	0.0638	0.71	1.0576	1.72	0.1203	1.57	732.7	9.0	732.3	10.9
XD-22	215	145	0.67	0.08	0.0637	1.10	1.0263	2.79	0.1169	2.56	717.1	14.5	712.8	17.3
Kawuliuke Fe-P deposit (GPS coordinate: 41°26′31.5″N, 86°34′03″E)														
KWLK-04	756	368	0.49	0.14	0.0671	0.59	1.2416	1.65	0.1364	1.51	819.6	9.3	824.2	11.7
KWLK-06	279	130	0.47	0.06	0.0668	1.06	1.2220	1.87	0.1335	1.50	810.7	10.5	807.8	11.4
KWLK-07	1252	207	0.17	1.89	0.0807	0.76	1.1965	1.95	0.1312	1.50	799.0	10.8	794.8	11.2
KWLK-08	1679	777	0.46	0.19	0.0673	0.40	1.2158	1.57	0.1339	1.50	807.9	8.8	810.1	11.4
KWLK-09	115	116	1.00	0.07	0.0668	1.76	1.2093	2.37	0.1323	1.51	804.8	13.2	800.9	11.4
KWLK-10	245	199	0.81	0.06	0.0663	1.06	1.2096	1.86	0.1332	1.50	805.0	10.4	806.2	11.4
KWLK-11	1466	1011	0.69	0.23	0.0685	0.42	1.2108	1.59	0.1316	1.51	805.6	8.9	797.1	11.3
KWLK-16	176	66	0.38	0.11	0.0668	1.17	1.2127	1.98	0.1335	1.50	806.4	11.1	807.6	11.4
KWLK-17	379	43	0.11	0.06	0.0655	0.80	1.2071	1.70	0.1337	1.50	803.9	9.5	809.0	11.4
KWLK-18	111	89	0.80	0.13	0.0663	1.47	1.1916	2.28	0.1324	1.50	796.7	12.7	801.4	11.3
KWLK-19	170	99	0.58	0.02	0.0663	1.22	1.2303	1.94	0.1348	1.50	814.5	11.0	815.4	11.5
KWLK-20	115	113	0.98	0.04	0.0667	1.64	1.2177	2.25	0.1330	1.50	808.7	12.6	804.7	11.4
KWLK-21	352	555	1.57	0.08	0.0659	0.87	1.2110	1.76	0.1332	1.53	805.6	9.8	806.3	11.6
KWLK-25	167	75	0.45	0.08	0.0665	1.56	1.2091	2.21	0.1332	1.50	804.8	12.4	806.3	11.4
KWLK-26	269	230	0.85	0.20	0.0676	0.93	1.2129	1.85	0.1332	1.50	806.5	10.3	805.9	11.4
KWLK-27	436	369	0.85	0.04	0.0666	0.73	1.2163	1.68	0.1330	1.50	808.1	9.4	805.0	11.4
KWLK-29	126	123	0.98	0.09	0.0659	1.35	1.2215	2.02	0.1345	1.50	810.5	11.3	813.5	11.5
Daxigou P-Fe deposit (GPS coordinate: 41°14′58″N, 87°29′46″E)														
DXG-2	376	100	0.27	0.00	0.1593	0.75	10.2314	2.06	0.4659	1.92	2455.9	19.3	2465.3	39.5
DXG-3	1038	84	0.08	0.00	0.1611	0.20	10.2484	1.52	0.4615	1.51	2457.5	14.2	2446.2	30.7
DXG-07	640	74	0.11	0.01	0.1593	0.21	10.1417	1.52	0.4618	1.51	2447.8	14.2	2447.5	30.8
DXG-10	294	93	0.31	0.02	0.1625	0.39	10.1295	1.55	0.4523	1.50	2446.7	14.4	2405.5	30.2
DXG-11	252	104	0.41	0.01	0.1602	0.45	10.0305	1.57	0.4541	1.51	2437.6	14.6	2413.6	30.4
DXG-13	675	79	0.12	0.00	0.1615	0.25	10.1336	1.52	0.4552	1.50	2447.0	14.2	2418.4	30.4
DXG-16	904	15	0.02	0.00	0.1604	0.35	10.1229	1.56	0.4577	1.52	2446.1	14.5	2429.4	30.8
DXG-17	156	82	0.53	0.02	0.1636	0.55	10.4987	1.60	0.4656	1.51	2479.8	15.0	2464.3	30.9
Qieganbulake (GPS coordinate: 41°13′27″N, 87°36′22″E)														
QGBLK-1	135	42	0.31	0.32	0.0663	1.23	1.2154	1.95	0.1330	1.52	807.7	10.9	805.0	11.5
QGBLK-2	3	7	2.84	3.46	0.0472	25.79	0.8706	25.84	0.1337	1.55	635.9	130.1	809.2	11.8
QGBLK-3	27	84	3.07	0.18	0.0659	2.70	1.2244	3.09	0.1348	1.50	811.8	17.4	815.4	11.5
QGBLK-4	32	16	0.50	0.41	0.0640	3.12	1.1554	3.47	0.1310	1.51	779.8	19.1	793.4	11.3
QGBLK-05	115	16	0.14	0.08	0.0659	1.26	1.1941	2.01	0.1313	1.56	797.9	11.2	795.5	11.7
QGBLK-06	86	36	0.42	0.10	0.0659	2.02	1.2000	2.52	0.1321	1.50	800.6	14.0	800.0	11.3
QGBLK-07	221	108	0.49	0.06	0.0555	1.39	0.5057	2.05	0.0661	1.51	415.5	7.0	412.7	6.0
QGBLK-8	208	1289	6.20	0.14	0.0659	0.89	1.2401	1.83	0.1366	1.60	818.9	10.3	825.2	12.4
QGBLK-9	248	890	3.59	0.10	0.0661	1.24	1.2206	1.95	0.1340	1.50	810.0	10.9	810.6	11.5
QGBLK-11	710	270	0.38	0.05	0.0516	1.02	0.3127	1.85	0.0439	1.54	276.3	4.5	277.0	4.2
QGBLK-12	53	90	1.68	0.06	0.0667	1.81	1.2604	2.35	0.1371	1.50	828.1	13.4	828.4	11.7
QGBLK-13	36	41	1.14	0.31	0.0645	2.24	1.1839	2.70	0.1331	1.50	793.1	15.0	805.8	11.4
QGBLK-14	59	31	0.54	0.32	0.0650	1.76	1.2104	2.31	0.1350	1.50	805.4	12.9	816.4	11.5
QGBLK-15	14	17	1.27	2.00	0.0648	4.02	1.1652	4.29	0.1305	1.52	784.4	23.7	790.4	11.3
QGBLK-16	15	6	0.41	0.09	0.0651	3.33	1.2293	3.66	0.1370	1.52	814.0	20.7	827.5	11.8
QGBLK-17	240	542	2.26	0.04	0.0664	1.07	1.2353	1.86	0.1349	1.52	816.7	10.5	815.9	11.7
QGBLK-18	632	1013	1.60	0.23	0.0663	0.73	1.1545	1.67	0.1264	1.50	779.3	9.1	767.1	10.9
QGBLK-19	97	245	2.51	0.32	0.0656	1.32	1.2095	2.00	0.1337	1.51	805.0	11.2	809.1	11.5
QGBLK-20	52	69	1.32	1.90	0.0621	6.22	1.1259	6.59	0.1315	2.19	765.8	36.1	796.6	16.4
QGBLK-21	106	240	2.26	0.32	0.0665	1.27	1.2402	1.97	0.1353	1.50	819.0	11.1	817.8	11.5

(continued on next page)

Please cite this article as: Han, C., et al., Ages and tectonic implications of the mafic–ultramafic-carbonatite intrusive rocks and associated Cu-Ni, Fe-P and apatite-vermic..., Ore Geol. Rev. (2016), http://dx.doi.org/10.1016/j.oregeorev.2016.07.011

Table 1 (*continued*)

Sample spot	U (ppm)	Th (ppm)	$\frac{Th}{U}$	f_{206}[a] (%)	$\frac{^{207}Pb}{^{206}Pb}$	±1σ (%)	$\frac{^{207}Pb}{^{235}Pb}$	±1σ (%)	$\frac{^{206}Pb}{^{238}Pb}$	±1σ (%)	$t_{207/235}$ (Ma)	±1σ	$t_{206/238}$ (Ma)	±1σ
QGBLK-22	117	264	2.26	0.08	0.0663	1.30	1.2290	1.98	0.1343	1.50	813.9	11.2	812.6	11.5
QGBLK-23	67	47	0.70	0.29	0.0680	1.56	1.2855	2.17	0.1371	1.51	839.3	12.5	828.5	11.8
QGBLK-24	56	51	0.90	0.19	0.0671	2.53	1.2573	2.98	0.1359	1.56	826.7	17.0	821.7	12.1
QGBLK-25	273	343	1.25	0.04	0.0660	0.79	1.2201	1.70	0.1340	1.51	809.8	9.5	810.9	11.5
QGBLK-26	171	725	4.23	0.08	0.0654	1.00	1.2176	1.84	0.1351	1.54	808.7	10.3	816.8	11.9

[a] f_{206} is the percentage of common ^{206}Pb in total ^{206}Pb.

5.1.2. Qieganbulake intrusion

Zircons are mostly small, subhedral to anhedral, and colorless, lacking inherited cores (Fig. 8). Most zircons have a wide range of variation in U and Th contents (3–710 ppm and 6–1289 ppm respectively) and high Th/U ratios (0.14–6.20) (Table 1). Twelve analyses of 25 zircon grains (Table 1) yielded a weighted mean $^{206}Pb/^{238}U$ age of 812 ± 5 Ma (2σ, MSWD = 0.74), and form a tight cluster on concordia (Fig. 9).

5.1.3. Daxigou intrusion

Zircons in this intrusion are mostly small and subhedral to anhedral (Fig. 8). Most zircons have high U and Th contents (156–1038 ppm and 15–104 ppm respectively) and high Th/U ratios (0.02–0.53) (Table 1). Twelve analyses of 8 zircon grains (Table 1) yielded a weighted mean $^{206}Pb/^{238}U$ age of 2452 ± 10 Ma (1σ, MSWD = 0.73) and form a tight cluster on concordia (Fig. 9).

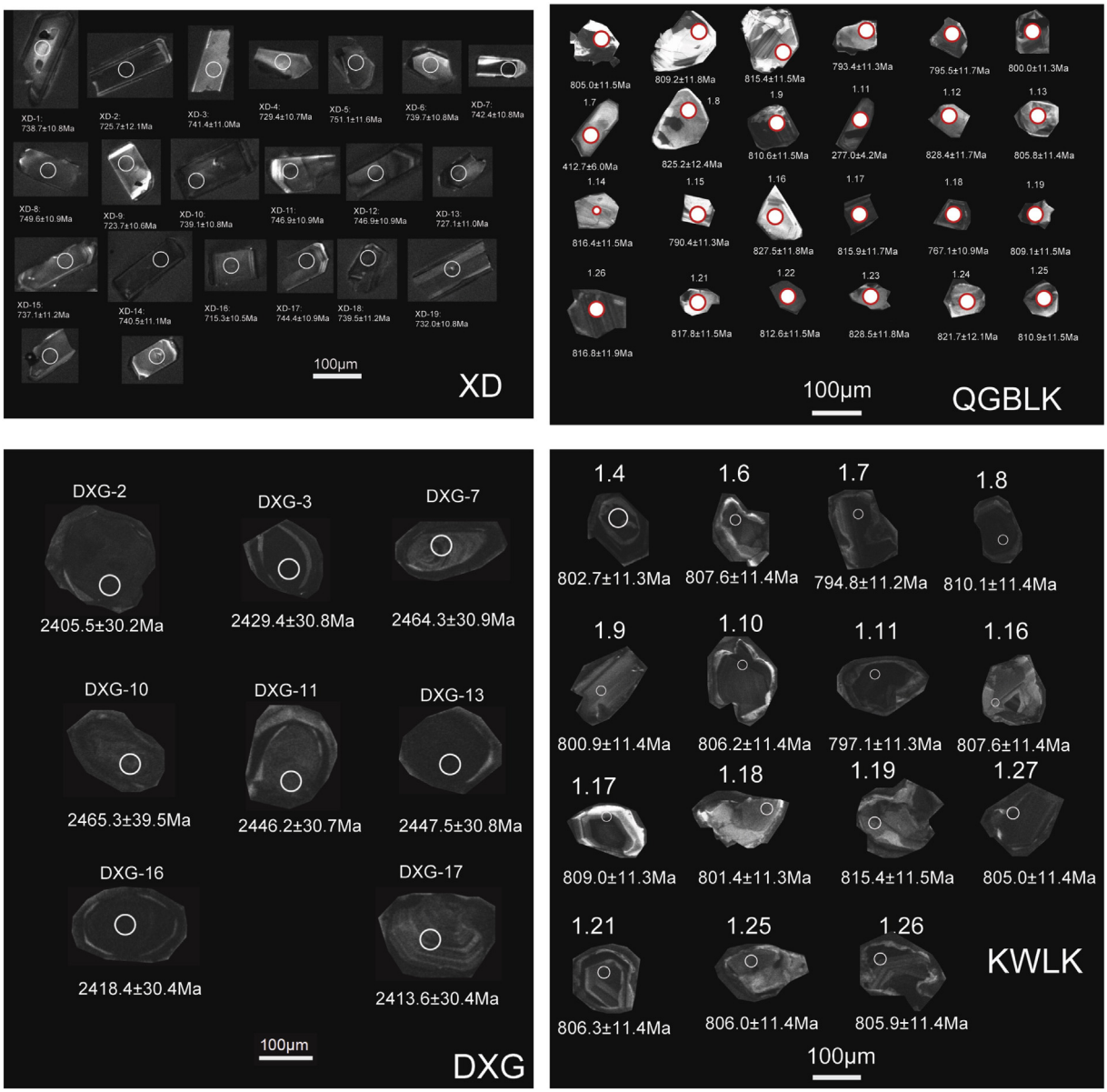

Fig. 8. Cathodoluminescence (CL) images of zircons from the mafic-ultramafic-carbonatite rcoks in the Quruqtagh domain, Xinjiang. Circles show the locations of SIMS U–Pb age isotope measurements, $^{206}Pb/^{238}U$ ages (Ma) are shown above and below the circles, respectively. XD = Xingdi gabbro, QGBLK = qieganbulake gabbro, DXG = the Daxigou gabbro, KWLK = Kawuliuke gabbro. Numbers refer to spots listed in Table 1.

Please cite this article as: Han, C., et al., Ages and tectonic implications of the mafic–ultramafic-carbonatite intrusive rocks and associated Cu-Ni, Fe-P and apatite-vermic..., Ore Geol. Rev. (2016), http://dx.doi.org/10.1016/j.oregeorev.2016.07.011

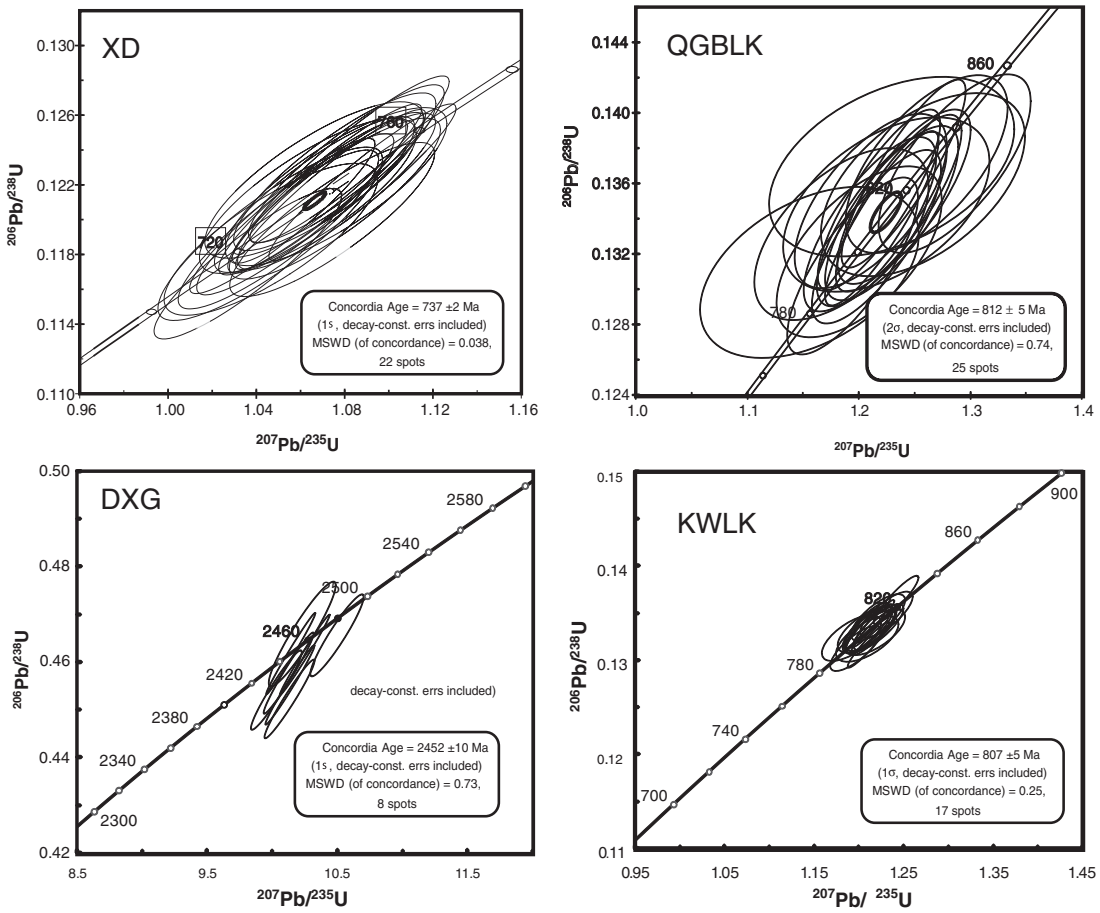

Fig. 9. Zircon U-Pb concordia diagrams for the dated mafic-ultramafic complexes in in the Quruqtagh domain, Xinjiang. XD = Xingdi gabbro, QGBLK = qieganbulake gabbro, DXG = Daxigou gabbro, KWLK = Kawuliuke gabbro.

5.1.4. Kawuliuke intrusion

The zircons are mostly small, subhedral to anhedral, and colorless, lacking inherited cores (Fig. 8). Most of the zircons have high U and Th contents (111–1679 ppm and 43–1011 ppm respectively) and high Th/U ratios (0.11–157) (Table 1). Twelve analyses of 17 zircon grains (Table 1) yielded a weighted mean $^{206}Pb/^{238}U$ age of 807 ± 5 Ma (1σ, MSWD = 0.25, and form a tight cluster on concordia (Fig. 9).

5.1.5. Qieganbulake intrusion

Zircon grains are mostly small, subhedral to anhedral and colorless. In CL images (Fig. 8), no inherited cores were observed. They have high U (3–710 ppm) and Th (40–459 ppm) contents, and high Th/U ratios (0.40–0.95) (Table 1). Such features indicate that they crystallized from magmas (Wu et al., 2006). Twelve analyses of 22 zircon grains (Table 1) yielded a weighted mean $^{206}Pb/^{238}U$ age of 737 ± 2 Ma (1σ, MSWD = 0.038, and form a tight cluster on concordia (Fig. 9).

5.2. Major- and trace-element geochemistry

The mafic and ultramafic rocks of Xingdi, Daxigou and Kawuliuke show a wide variation in their major oxide concentrations (Table 2). These samples have a wide range of SiO_2 (27.76–59.57%, average 44.45%), MgO (2.94–25.35%, average 9.88%) and Al_2O_3 (7.84–16.84%, average 12.06%), CaO (6.51–14.79%, average 10.29%) contents, but show relatively low TiO_2 (0.24–4.58%, average 0.49%) and P_2O_5 (0.03–2.61%, average 0.69%) (Table 2).

The diagrams of MgO versus major oxides and compatible elements exhibit evidence for the fractionation/accumulation of olivine, pyroxenes, and plagioclase. For example, a negative correlation of MgO with Al_2O_3, SiO_2, TiO_2 and CaO indicates fractionation/accumulation of olivine, pyroxenes and/or plagioclase, whereas a positive correlation of MgO with compatible elements (e.g. Cr, Co and Ni) is consistent with fractionation/accumulation of olivine and orthopyroxene (Fig. 10).

All the samples from Xingdi have variable REE contents, reflecting different abundances and compositions of intercumulus liquids as well as distinct fractionation/accumulation histories, but are all enriched in LREE relative to HREE ($(La/Yb)_N$ = 2.40–9.14) with flat HREE patterns ($(Gd/Yb)_N$ = 1.42–1.68) (Fig. 11; Table 2). Most of the samples show slightly negative or positive Eu anomalies (Eu/Eu^* = 0.90 to 1.23), which may be attributed to the fractionation or accumulation of plagioclase, respectively. The patterns from Kawuliuke are enriched in REE and show LREE/HREE enrichment ($(La/Yb)_N$ = 8.59–51.04), while the Daxigou patterns also show LREE/HREE enrichment ($(La/Yb)_N$ = 6.76–31.84) (Fig. 11; Table 2). The Kawuliuke and Daxigou samples display small negative Eu anomalies (Eu/Eu^* = 0.80–0.92 and 0.62–0.99, respectively).

The primitive mantle-normalized trace-element diagrams exhibit variable abundances of elements (Fig. 12), and most Xingdi samples show pronounced negative Th, Nb, Ta, Pr and Zr anomalies, coupled with enrichments in Ba, U, La, Ce and Sr relative to their neighboring elements, due to fractional crystallization and/or mineral accumulation. Other notable features of Poshi and Luodong samples include depletion of Th relative to Ba, enriched Pb and Sr relative to Ce and Nd, and depleted Zr relative to Nd (Fig. 12).

Table 2
Major and trace-element data of the Kawuliuke deposit and Daxigou deposit.

Sample no.	KWLK-12	KWLK-13	KWLK-14	KWLK-15	KWLK-16	KWLK-17	KWLK-18	KWLK-19	KWLK-20	KWLK-21	KWLK-22	KWLK-23
Kawuliuke intrusion												
Rock type	Hornblende Gabbro					Gabbro			Pyroxenite			Gabbro
SiO_2	46.71	46	45.69	50.34	45.57	43.82	43.97	44.42	27.36	35.75	32.03	43.77
TiO_2	1.27	1.32	1.4	1.05	1.37	1.49	1.41	2.11	3.93	2.75	3.2	1.29
Al_2O_3	15.86	15.97	15.47	16.53	16	15.53	16.13	9.94	7.84	8.95	7.84	7.00
MnO	0.19	0.19	0.16	0.18	0.18	0.2	0.19	0.17	0.23	0.16	0.19	0.18
MgO	5.65	5.78	5.75	2.94	5.69	6.22	5.91	9.81	8.3	11.62	8.92	13.16
CaO	9.86	10.36	11.04	8.9	10.61	11.44	11.66	10.95	11.19	11.53	13.07	16.49
Na_2O	3.18	3.08	3.22	4.11	2.88	2.87	3.1	1.86	1.13	1.52	1.23	1.22
K_2O	1.51	1.18	0.94	2.25	1.44	1.29	0.87	1.15	0.64	0.67	0.65	0.43
P_2O_5	0.74	0.75	0.71	0.74	0.74	0.77	0.78	0.14	1.99	0.16	1.94	0.5
TFe_2O_3	13.23	13.39	13.28	10.14	13.25	14.44	13.79	17.83	36.1	25.47	28.88	13.7
LOI	1.34	1.68	0.68	1.08	1.14	1.28	1.48	1.38	0.40	0.68	0.50	0.73
Total	99.87	100.01	98.61	98.96	99.2	99.66	99.57	100.08	99.23	99.44	98.65	98.63
La	121.45	58.30	52.23	109.38	58.51	53.35	54.68	20.09	30.11	13.39	32.94	17.68
Ce	215.01	121.04	108.25	227.97	122.19	116.27	115.44	40.68	71.32	35.67	76.24	47.67
Pr	24.90	16.41	15.24	28.86	16.69	16.61	16.19	6.04	10.96	5.98	11.53	8.11
Nd	88.31	64.23	61.74	110.52	67.63	67.72	65.43	26.43	49.14	28.23	50.95	37.60
Sm	13.98	12.52	12.13	19.64	12.53	13.48	13.05	6.52	11.26	7.16	11.77	9.10
Eu	3.54	3.17	3.26	4.84	3.19	3.35	3.39	1.60	2.66	1.90	2.85	2.26
Gd	9.80	8.83	8.91	14.02	9.08	9.50	9.25	4.94	8.52	5.61	8.96	6.84
Tb	1.10	1.05	1.07	1.63	1.10	1.14	1.09	0.63	1.02	0.70	1.07	0.84
Dy	5.03	4.75	4.85	7.26	5.06	5.33	5.17	3.00	4.65	3.30	4.90	3.94
Ho	0.86	0.84	0.85	1.22	0.89	0.95	0.93	0.51	0.82	0.57	0.84	0.69
Er	2.08	2.13	2.16	2.95	2.20	2.37	2.28	1.25	1.85	1.36	1.96	1.65
Tm	0.28	0.28	0.28	0.40	0.30	0.31	0.30	0.17	0.23	0.18	0.25	0.22
Yb	1.61	1.71	1.68	2.41	1.80	1.83	1.81	1.01	1.30	1.05	1.38	1.28
Lu	0.22	0.24	0.23	0.35	0.25	0.26	0.26	0.14	0.18	0.14	0.19	0.18
∑REE	488.17	295.50	272.87	531.44	301.40	292.48	289.26	113.01	194.02	105.25	205.83	138.04
(Eu/Eu)*	0.88	0.88	0.92	0.85	0.87	0.86	0.9	0.83	0.8	0.88	0.82	0.84
(La/Yb)N	51.04	22.99	21.07	30.68	21.96	19.7	20.47	13.46	15.66	8.59	16.16	9.36
(La/Sm)N	5.47	2.93	2.71	3.51	2.94	2.49	2.64	1.94	1.68	1.18	1.76	1.22
(Gd/Yb)N	4.94	4.18	4.31	4.72	4.09	4.21	4.15	3.97	5.32	4.31	5.27	4.34
Sc	29	31	33	14	31	34	32	62	56	75	60	68
V	264	276	292	190	280	304	301	573	691	816	572	316
Cr	26	26	19	4	20	25	46	34	13	122	35	555
Co	35	34	38	21	36	39	38	68	83	83	67	53
Ni	24	18	22	9	33	18	42	118	37	117	32	93
Ga	23	23	23	23	23	23	24	19	25	19	21	13
Rb	28.2	26.8	16.4	37.5	30.8	24.8	12.2	12.7	4.9	3.7	5.9	3.3
Sr	1386	1688	1616	2576	1586	1523	1965	890	392	428	580	453
Y	23	23	23	34	24	25	24	13	19	14	20	17
Zr	45	51	44	172	52	47	49	48	41	33	41	42
Nb	15	11	10	35	11	11	12	12	8	6	8	6
Ba	1380	1030	809	4539	1411	1179	715	1760	290	368	817	273
Hf	1.5	1.6	1.5	5.0	1.7	1.6	1.7	1.9	1.5	1.3	1.6	1.6
Ta	0.40	0.47	0.43	2.03	0.51	0.49	0.50	0.52	0.41	0.31	0.39	1.00
Pb	7.8	7.8	8.5	16.4	8.2	5.4	9.2	5.1	5.3	4.6	5.3	5.0
Th	4.2	1.6	1.7	5.2	1.6	0.8	1.0	5.9	1.2	0.8	1.5	0.6
U	0.4	0.4	0.8	1.4	0.3	0.3	0.6	2.9	0.4	0.3	0.4	0.2

Sample no.	DXG-01	DXG-02	DXG-03	DXG-06	DXG-07	DXG-08	DXG-09	DXG-10	DXG-15	DXG-16	DXG-17
Daxigou intrusion											
Rock type	Hornblendite				Gabbro						
SiO_2	41.47	40.57	40.13	43.63	49.19	49.12	50.03	49.82	50.06	59.57	41.28
TiO_2	4.58	4.24	4.67	0.4	0.59	0.9	0.97	0.98	0.62	0.38	3.78
Al_2O_3	11.13	11.25	11.47	9.28	12.54	12.78	16.84	16.64	16.47	13.5	11.49
MnO	0.2	0.19	0.27	0.16	0.17	0.16	0.13	0.12	0.08	0.15	0.12
MgO	5.3	5.42	4.86	2.34	0.99	1.54	3.62	4.02	0.55	0.45	4.12
CaO	7.77	10.31	7.14	14.32	14.79	12.95	8.43	7.76	11.53	9.01	13.97
Na_2O	2.28	2.31	2.59	0.8	1.04	0.44	4.2	4.1	4.46	1.87	0.55
K_2O	0.73	0.23	0.96	2.46	3.15	3.9	1.28	1.27	2.61	3.25	0.15
P_2O_5	2.61	2.41	2.72	0.14	0.26	0.39	0.27	0.26	0.46	0.11	2.5
TFe_2O_3	22.2	19.19	23.12	6.11	5.23	4.91	8.43	8.59	3.67	3.51	18.62
LOI	1.12	3.02	1.53	16.53	11.66	12.17	5.12	6.07	9.30	7.15	2.36
Total	99.57	99.28	99.65	96.25	99.69	99.39	99.5	99.8	99.91	99.05	99.17
La	110.35	117.68	116.08	20.47	25.03	37.40	24.09	26.87	37.86	16.98	119.159
Ce	238.94	255.94	264.80	39.75	48.16	80.01	50.79	55.04	76.81	33.00	255.068
Pr	30.22	32.55	34.32	5.00	6.08	10.04	6.99	7.50	9.98	4.20	32.826
Nd	114.54	123.33	131.48	18.62	22.65	37.34	28.56	29.94	37.57	16.06	126.317
Sm	18.53	21.05	22.78	3.93	4.48	6.81	6.26	6.36	6.92	2.78	22.492

Please cite this article as: Han, C., et al., Ages and tectonic implications of the mafic–ultramafic-carbonatite intrusive rocks and associated Cu-Ni, Fe-P and apatite-vermic..., Ore Geol. Rev. (2016), http://dx.doi.org/10.1016/j.oregeorev.2016.07.011

Table 2 (*continued*)

Sample no.	DXG-01	DXG-02	DXG-03	DXG-06	DXG-07	DXG-08	DXG-09	DXG-10	DXG-15	DXG-16	DXG-17
Daxigou intrusion											
Rock type	Hornblendite				Gabbro						
Eu	3.68	4.42	4.10	1.17	1.30	1.82	1.68	1.72	1.77	0.83	4.956
Gd	13.38	15.12	16.19	3.57	3.45	5.02	5.56	5.54	5.00	2.21	15.994
Tb	1.56	1.75	1.87	0.56	0.47	0.67	0.83	0.82	0.59	0.31	1.862
Dy	7.37	8.19	8.77	3.35	2.31	3.48	4.66	4.64	2.75	1.63	9.197
Ho	1.28	1.47	1.57	0.69	0.41	0.64	0.92	0.94	0.50	0.30	1.646
Er	3.18	3.49	3.62	1.90	1.06	1.63	2.58	2.52	1.20	0.79	3.849
Tm	0.40	0.43	0.46	0.29	0.16	0.24	0.39	0.37	0.18	0.12	0.483
Yb	2.34	2.52	2.71	1.96	0.96	1.49	2.41	2.41	1.13	0.81	2.766
Lu	0.34	0.36	0.38	0.30	0.14	0.23	0.37	0.36	0.17	0.13	0.39
∑REE	546.11	588.29	609.12	101.56	116.67	186.81	136.09	145.04	182.43	80.14	597.01
(Eu/Eu)*	0.68	0.72	0.62	0.94	0.98	0.91	0.85	0.87	0.88	0.99	0.76
(La/Yb)N	31.84	31.56	28.97	7.06	17.56	16.98	6.76	7.52	22.72	14.23	29.11
(La/Sm)N	3.75	3.52	3.21	3.28	3.51	3.46	2.42	2.66	3.44	3.84	3.33
(Gd/Yb)N	4.63	4.86	4.85	1.48	2.9	2.74	1.87	1.86	3.6	2.22	4.69
Sc	30	27	33	10	13	14	26	25	11	6	27
V	403	361	396	56	92	127	186	184	67	46	364
Cr	97	70	76	66	112	102	43	43	65	49	58
Co	47	41	49	18	19	40	23	21	9	8	46
Ni	60	53	60	55	64	41	54	62	29	26	47
Ga	22	24	23	14	17	21	21	20	18	17	27
Rb	12.9	3.3	14.5	68.8	83.7	102.2	22.3	22.9	67.3	80.8	2.0
Sr	528	712	515	158	113	141	611	592	267	129	1675
Y	34	38	40	18	12	17	25	25	13	8	41
Zr	139	139	175	122	90	130	134	129	250	123	101
Nb	19	19	20	7	4	12	7	7	6	7	17
Ba	703	144	819	338	503	731	691	734	478	514	59
Hf	3.4	3.3	4.1	3.0	2.2	3.1	3.5	3.3	6.4	3.2	2.6
Ta	0.95	0.89	0.96	0.37	0.19	0.53	0.50	0.47	0.29	0.36	0.81
Pb	3.3	2.8	2.5	9.5	3.3	3.4	4.7	4.6	2.9	2.4	3.0
Th	2.8	1.4	1.7	2.1	0.5	5.8	1.3	1.2	3.1	1.9	2.0
U	0.6	0.4	0.5	1.0	0.6	0.7	0.4	0.5	1.1	0.8	0.4

Sample no.	XD1	XD2	XD3	XD4	XD5	XD6	XD7	XD8	XD9	XD10
Daxigou intrusion										
Rock type	Gabbro									
SiO_2	50.07	43.57	50.66	41.49	42.95	46.16	42.11	42.15	44.32	43.38
TiO_2	0.63	0.26	0.69	0.18	0.35	1.49	0.31	0.3	0.25	0.24
Al_2O_3	11	10.73	10.85	8.89	8.05	11.22	9.79	9.75	10.76	10.67
MnO	0.15	0.15	0.14	0.15	0.16	0.15	0.15	0.15	0.15	0.18
MgO	12.61	20.91	12.94	25.35	23.92	17.56	23.42	23.34	21.86	21.31
CaO	12.37	7.92	12.84	5.84	7.95	8.67	6.51	6.83	7.88	7.88
Na_2O	1.47	1.38	1.43	1.03	1.01	1.67	1.13	1.15	1.35	1.3
K_2O	0.51	0.21	0.42	0.13	0.17	0.67	0.18	0.16	0.18	0.21
P_2O_5	0.03	0.04	0.04	0.03	0.05	0.37	0.06	0.05	0.04	0.04
TFe_2O_3	8.21	9.31	7.81	10.31	9.97	9.83	10.07	10	9.44	9.54
LOI	1.46	3.32	1.28	4.48	3.54	1.52	4.38	4.38	3.08	3.56
Total	98.5	97.81	99.1	97.88	98.12	99.31	98.11	98.25	99.32	98.31
La	5.3	3.1	5.4	1.9	3.6	23.8	2.9	2.6	2.9	2.9
Ce	12.6	6.2	12.8	4.1	7.8	54	6.5	5.9	5.9	5.8
Pr	2	0.84	2.07	0.59	1.16	7.62	0.94	0.85	0.8	0.79
Nd	9.43	3.69	10.26	2.61	5.32	31.16	4.29	3.87	3.46	3.4
Sm	2.7	0.95	2.81	0.74	1.44	6.13	1.1	1.07	0.92	0.93
Eu	0.89	0.39	0.88	0.3	0.5	1.71	0.43	0.42	0.38	0.39
Gd	2.9	1.1	2.9	0.8	1.6	5.3	1.2	1.1	1	1
Tb	0.48	0.18	0.51	0.13	0.27	0.77	0.2	0.19	0.16	0.16
Dy	2.96	1.1	3.04	0.81	1.71	4.09	1.23	1.18	1.06	1.05
Ho	0.6	0.23	0.62	0.17	0.36	0.79	0.26	0.25	0.22	0.21
Er	1.59	0.62	1.64	0.46	0.95	2.01	0.7	0.68	0.6	0.59
Tm	0.24	0.08	0.24	0.07	0.14	0.28	0.11	0.1	0.09	0.08
Yb	1.49	0.53	1.47	0.41	0.86	1.76	0.66	0.63	0.56	0.5
Lu	0.21	0.08	0.21	0.06	0.12	0.24	0.10	0.09	0.08	0.07
∑REE	43.39	19.09	44.85	13.15	25.83	139.66	20.62	18.93	18.13	17.87
(Eu/Eu)*	0.97	1.16	0.93	1.19	1	0.9	1.14	1.17	1.2	1.23
(La/Yb)N	2.4	3.95	2.48	3.13	2.83	9.14	2.97	2.79	3.5	3.92
(La/Sm)N	1.24	2.05	1.21	1.62	1.57	2.44	1.66	1.53	1.98	1.96
(Gd/Yb)N	1.58	1.68	1.6	1.58	1.51	2.44	1.47	1.42	1.45	1.62
Sc	44	23	45	17	30	28	20	20	23	23
V	189	85	193	66	117	194	84	84	84	84
Cr	1017	1899	1027	2125	3030	1634	2075	2177	1978	1921

(*continued on next page*)

Please cite this article as: Han, C., et al., Ages and tectonic implications of the mafic–ultramafic-carbonatite intrusive rocks and associated Cu-Ni, Fe-P and apatite-vermic..., Ore Geol. Rev. (2016), http://dx.doi.org/10.1016/j.oregeorev.2016.07.011

Table 2 (*continued*)

Sample no.	XD1	XD2	XD3	XD4	XD5	XD6	XD7	XD8	XD9	XD10
Daxigou intrusion										
Rock type	Gabbro									
Co	43	74	43	92	85	66	88	87	79	79
Ni	112	433	127	598	554	401	534	526	475	470
Ga	12	8	12	7	7	14	8	8	8	8
Rb	15.4	6.5	14.7	3.5	6.2	17.5	5.6	6.6	6.0	6.2
Sr	322	243	306	171	201	438	219	221	239	294
Y	15	6	15	5	9	20	7	6	6	6
Zr	37	22	39	21	41	166	29	28	26	22
Nb	2	1	2	1	2	7	2	2	1	1
Ba	157	109	129	50	101	294	77	75	96	166
Hf	1.3	0.6	1.3	0.6	1.1	4.3	0.8	0.8	0.7	0.6
Ta	0.09	0.09	0.10	0.08	0.10	0.40	0.10	0.09	0.09	0.09
Pb	8.4	14.1	6.1	3.3	22.5	4.5	9.5	12.0	10.8	30.1
Th	0.7	0.5	0.5	0.3	0.5	1.3	0.3	0.5	0.6	0.5
U	0.3	0.2	0.3	0.1	0.3	0.4	0.3	0.3	0.2	0.2

LOI = Loss on Ignition.

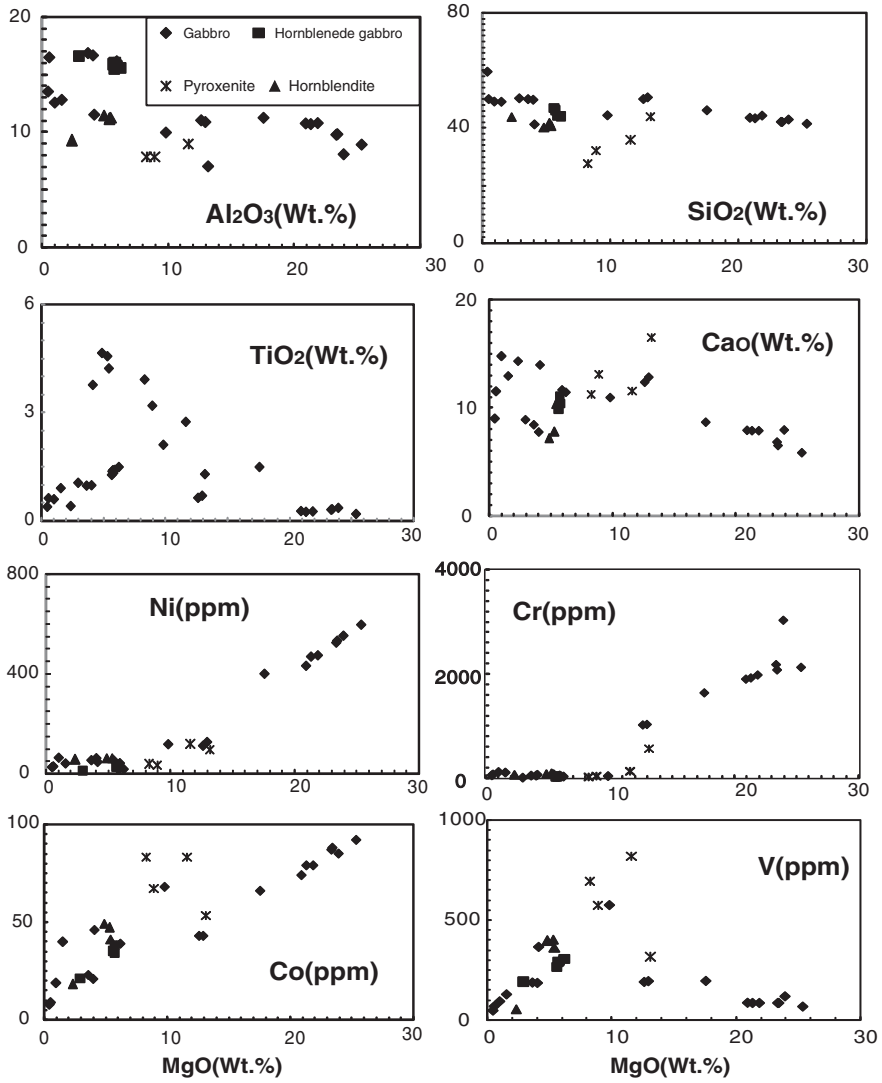

Fig. 10. Diagrams of MgO versus major oxides and compatible elements for the Xingdi (XD), Daxigou (DXG) and Kawuliuke (KWLK) complexes.

Please cite this article as: Han, C., et al., Ages and tectonic implications of the mafic–ultramafic-carbonatite intrusive rocks and associated Cu-Ni, Fe-P and apatite-vermic..., Ore Geol. Rev. (2016), http://dx.doi.org/10.1016/j.oregeorev.2016.07.011

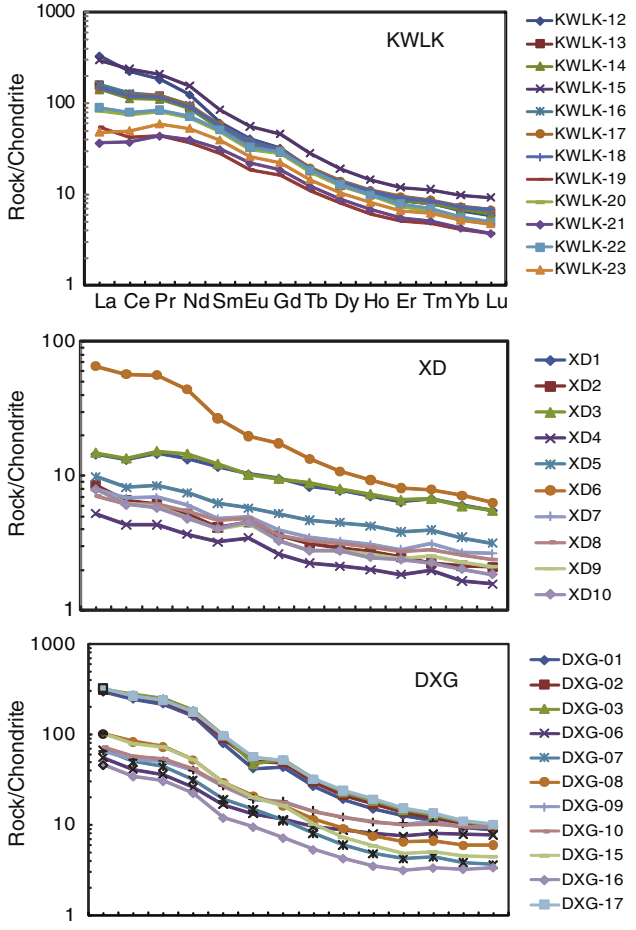

Fig. 11. Chondrite-normalized REE patterns from a suite of rocks of the Xingdi (XD), Daxigou (DXG) and Kawuliuke (KWLK) complexes (normalizing values are from Sun and McDonough, 1989).

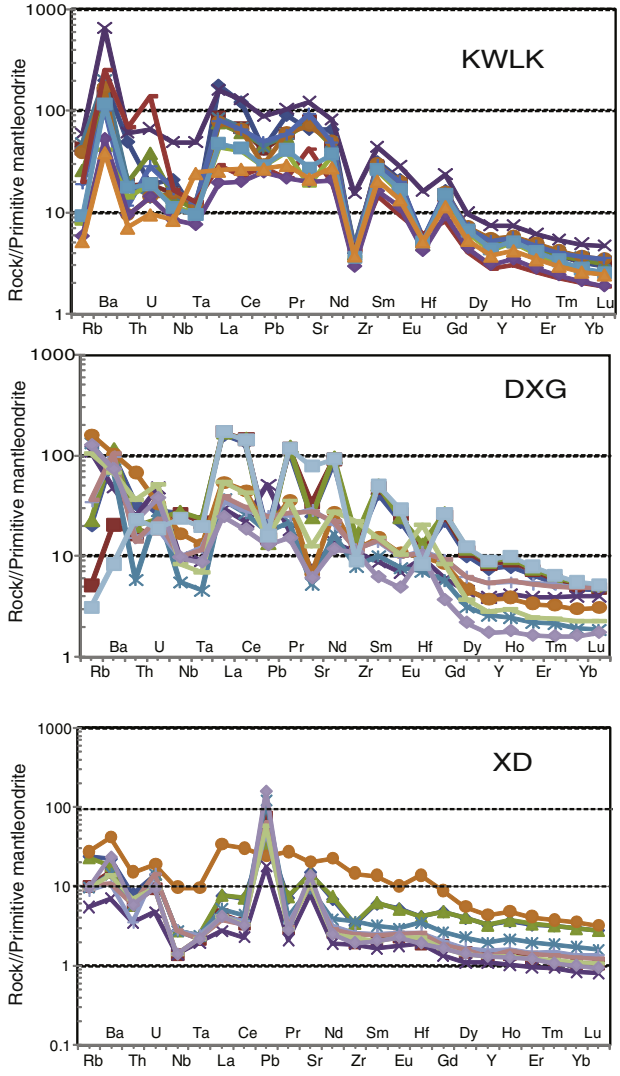

Fig. 12. Primitive mantle-normalized spidergrams for the three studied of the Xingdi (XD), Daxigou (DXG) and Kawuliuke (KWLK) complexes (normalizing values are from Sun and McDonough, 1989).

6. Discussion

6.1. Geochronological framework

Extensive magmatism (ca. 2450–600 Ma) has been documented in the Tarim Craton (Table 3; Xu et al., 2005; Zhang et al., 2007; Xu et al., 2009; Cao et al., 2011; Long et al., 2011; Shu et al., 2011; Zhang et al., 2011; Ge et al., 2012). A compilation of published high-quality geochronological data, mainly in situ zircon U-Pb data, minor $^{39}Ar/^{40}Ar$, Sm-Nd and Re-Os data, with the present data will enable us to subdivide magmatism of this age into six distinct magmatic episodes as follows: (1) ca. 2450–2350 Ma; (2) ~1900 Ma; (3) ca. 1050–900 Ma; (4) ca. 830–790 Ma; (5) ca. 760–730 Ma; (6) ca. 660–630 Ma. Since this represent the period of assembly and separation of the Rodinia supercontinent, as well as the commencement of amalgamation of the Gondwana supercontinent, the geological significance of these episodes of magmatic events is discussed in the context of supercontinental circles.

The 2.45–2.35 Ga magmatic event was also represented by the emplacement of trondhjemites and mafic dykes in the eastern Altyn Tagh of the Dunhuang Complex, of which the mafic dykes have been metamorphosed into garnet amphibolites. Igneous zircons from the trondhjemite and mafic dyke (garnet amphibolite) yielded U-Pb ages of 2374 ± 10 Ma and 2351 ± 21 Ma, respectively (Lu, 2002), indicating that they were emplaced coevally. This data led Lu et al. (2008) to interpret them as a result of bimodal magmatism related to an intracontinental rifting event in the early Paleoproterozoic. As mentioned above, associated with Neoarchean and Paleoproterozoic plutonic rocks in the Dunhuang Complex are Paleoproterozoic supracrustals (the Dunhuang supracrustals), including garnet-sillimanite quartz schist, garnet-sillimanite-mica schist, garnet–sillimanite gneiss, amphibolites and marble, which have not been well dated in terms of their protolithic and depositional ages, though metamorphic zircons from a mafic granulite sample yielded a SHRIMP U-Pb age of 1818 ± 16 Ma, interpreted as the time of the granulite facies metamorphism (Zhang et al., 2012a, 2012b).

A 1.9 Ga magmatic event has been established from the Paleoproterozoic Xingtage gneissic granites in the Quruqtagh Complex on the northeastern margin of the Tarim Craton (Zhang et al., 2007; Shu et al., 2011 where obtained a LA-ICP-MS U—Pb zircon age of 1943 ± 6 Ma for a granitic gneiss and Zhang et al. (2007) also obtained an U-Pb zircon age of 1916 ± 7 Ma for high-K granite. Long et al. (2012) carried out geochemical and zircon U-Pb dating and Hf isotope studies on the Paleoproterozoic Xinger gneissic granite in the Quruqtagh Complex. Geochemically, the Xinger granite is high in SiO_2 (75.45–78.49 wt.%), $K_2O + Na_2O$ (6.38–9.00 wt.%), and high field strength elements, and shows significant negative Eu anomalies, typical of A-type peraluminous granites (Long et al., 2012). The zircon dating result indicates that the Xinger gneissic granite was emplaced at 1915 ± 13 Ma, and the εHf(t) values of the granite range between −13 and −8 (Long et al., 2012), suggesting a derivation from the partial melting of Archean

Table 3
Compilation of the geochronological data from the Tarim Cratont.

Location	Lithology	Age(Ma)	Method	References
Dapingliang	Plagiogranite	826 ± 13	LA-ICP-MS	Cao et al. (2010)
Dapingliang	Molybdenite	830 ± 26	Re-Os isochron	Cao et al. (2010)
Dapingliang	K-feldspar granite	816.2 ± 4.6	LA-ICP-MS	Cao et al. (2011)
Central QU	Biotite granite	798 ± 3	LA-ICP-MS	Long et al. (2011)
Central QU	Quartzdiorite	754 ± 4	LA-ICP-MS	Long et al. (2011)
Central QU	Biotite granodiorite	790 ± 3	LA-ICP-MS	Long et al. (2011)
Central QU	Granodiorite	785 ± 8	LA-ICP-MS	Long et al. (2011)
Xishankou, QU	Tuff	755 ± 15	SHRIMP	Xu et al. (2005)
Saimashan	Volcanics	732 ± 7	SHRIMP	Xu et al. (2008)
Xinger	Rhyolite	740 ± 15	SHRIMP	Xu et al. (2009)
Xishankou, QU	Basalts	725 ± 10	SHRIMP	Xu et al. (2009)
Mochia-Khutuk	Andesite	615 ± 6	SHRIMP	Xu et al. (2009)
No 1 biomodel complex	Gabbro	735.2 ± 4.2	SIMS	Zhang et al. (2011)
No 1 biomodel complex	Olivine Gabbro	734.8 ± 3.6	SIMS	Zhang et al. (2011)
No 1 biomodel complex	Granite	737.3 ± 4.5	SIMS	Zhang et al. (2011)
No IV biomodel complex	Gabbro	736.4 ± 4.9	SIMS	Zhang et al. (2011)
No IV biomodel complex	Granite	734.1 ± 4.1	SIMS	Zhang et al. (2011)
Zhongtuzhan	Ultramafic dyke	802.1 ± 6.1	SIMS	Zhang et al. (2011)
Taiyangdao	Noritic gabbro	760 ± 6	SHRIMP	Zhang et al. (2011)
Qieganbulake	Carbonatite	810 ± 6	TIMS	Zhang et al. (2007)
Qieganbulake	Phlogopitelite	812 ± 1.2	Ar-Ar	Zhang et al. (2007)
Qieganbulake	Pyroxenite	818 ± 11	SHRIMP	Zhang et al. (2007)
Qieganbulake	Whole rock	800 ± 25	Sm-Nd	Zhang et al. (2007)
Xingdi	Granodiorite	820 ± 10	SHRIMP	Zhang et al. (2007)
Taiyangdao	Granite	795 ± 10	SHRIMP	Zhang et al. (2007)
Kudi	Granite	815 ± 57	SHRIMP	Zhang et al. (2003)
Taiyangdao	Dolerite	773 ± 3	TIMS	Zhang et al. (2009a)
Aksu	Gabbro	759 ± 7	SHRIMP	Zhang et al. (2009a)
Xuxugou	Gabbro	802 ± 9	SHRIMP	Zhang (2010)
Central QU	Diabase	823.8 ± 8.7	SHRIMP	Zhang et al. (2009b)
Central QU	Diabase	776.8 ± 8.9	SHRIMP	Zhang et al. (2009b)
Kudi	Granite	783 ± 10	SHRIMP	Zhang et al. (2006)
Xingdi	Granite	798 ± 7	LA-ICP-MS	Deng et al. (2008)
Xingdi	Diabase	816 ± 15	LA-ICP-MS	Deng et al. (2008)
Xingdi	Granite	798 ± 7	LA-ICP-MS	Deng et al. (2008)
Xingdi	Diabase	806 ± 8	LA-ICP-MS	Shu et al. (2011)
TC-1 Well	Diorite	790 ± 22	Ar-Ar	Guo et al. (2005)
TC-1 Well	Diorite	754 ± 23	Ar-Ar	Guo et al. (2005)
TC-1 Well	Diorite	744 ± 9.3	Ar-Ar	Guo et al. (2005)
Central QU	Pillow basalt	705 ± 10	SHRIMP	Cao et al. (2010)
Central QU	Volcanics	739 ± 6	SHRIMP	Cao et al. (2010)
TC-1 Well	Granodiorite	757.4 ± 6.2	SHRIMP	Xu et al. (2009)
Taiyangdao	Granite	795 ± 10	SHRIMP	Luo et al. (2011)
Korla	Spessartite	628.7 ± 6.6	SHRIMP	Zhu et al. (2008)
Korla	Diabase	652.0 ± 7.4	SHRIMP	Zhu et al. (2008)
Korla	Diabase	642.8 ± 6.9	SHRIMP	Zhu et al. (2008)
Korla	Spessartite	634.0 ± 6.0	SHRIMP	
Tugering	Granite	636.4 ± 4.5	SHRIMP	
Tugering	Granite	631.4 ± 3.5	SHRIMP	
Tugering	Granite	631.4 ± 3.5	SHRIMP	

QU = Quruqtagh.

TTG gneisses. Long et al. (2012) postulated that this partial melting event was coincident with the global collisional events that led to the assembly of the Paleo-Mesoproterozoic Columbia (Nuna) supercontinent.

The ca. 1050–900 Ma magmatism includes 1050–1021 Ma metavolcanics ($^{39}Ar/^{40}Ar$ hornblende and biotite) in west Kunlun (Zhang et al., 2003), 1048 ± 19 Ma gnessic granite in the central Kuruktag (Shu et al., 2011) and 950–900 Ma granitoids and metarhyolite around Tarim (Gehrels et al., 2003; Shu et al., 2011). This magmatism was generally interpreted as a Grenvillian event resulting in the assembly of Tarim to Rodinia. It is worth noting, however, that magmatic rocks of this age are relatively sparse and few geochemical data are available to evaluate their significance. Their ages are obviously younger than typical Grenvillian (1300–1100 Ma) events. Furthermore, few detrital zircons of this age have been revealed in recent studies (e.g., Zhang et al., 2011), suggesting that Grenvillian events are probably insignificant in the northern Tarim Craton. The Tarim Orogeny, leading to the final cratonization of the Tarim (Gao et al., 1993; Lu et al., 2008), was believed to be Grenvillian in age (e.g., Lu et al., 2008; Shu et al., 2011; Zhang et al., 2012a, 2012b), but the time, tectonic significance and correlation with other Grenvillian orogenic belts are still uncertain. Therefore, when, how and where did the Tarim Craton join the Rodinia still remain subjects of continuous debate (Huang et al., 2005; Zhang et al., 2007; Lu et al., 2008).

The ca. 830–730 Ma magmatism includes mafic to ultramafic dyke swarms (Zhang et al., 2011), carbonatite-ultramafic-mafic intrusion complexes (Zhang et al., 2007, 2011), bimodal intrusion complexes (Zhang et al., 2006), volcanic layers interbeded within rift sequences (Xiao et al., 2004; Xu et al., 2009) and various granitoids (Zhang et al., 2007, 2011; Cao et al., 2010; Long et al., 2011). They are relatively well documented in the Quruqtagh Uplift in the northern Tarim Craton. Current geochronological data define two broad magmatic peaks: ca. 830–790 Ma and ca. 760–730 Ma, although sub-peaks may be recognized (Zhang et al., 2011). These rocks are generally interpreted as products of extension or rifting related to the breakup of Rodinia, although whether or not this extension or rifting led to the separation of Tarim from Rodinia is uncertain, as no breakup unconformity or other geological or paleomagnetic evidence have been documented. Two episodes of

Please cite this article as: Han, C., et al., Ages and tectonic implications of the mafic–ultramafic-carbonatite intrusive rocks and associated Cu-Ni, Fe-P and apatite-vermic..., Ore Geol. Rev. (2016), http://dx.doi.org/10.1016/j.oregeorev.2016.07.011

mantle superplume activities that probably led to the breakup of Rodinia (Li et al., 1999, 2003a, 2003b, 2008) are the most popular models to explain the diverse magmatism in the Tarim. However, it should be pointed out that most igneous rocks exhibit arc signatures, such as enrichment of LREE and LILE and Nb-Ta-Ti depletion, and OIB-like magmatism is only documented in the southern Tarim (Zhang et al., 2011). As the northern Tarim Craton faced the exterior ocean surrounding the Rodinia supercontinent, we suggested that the subduction of this ocean may have played an irreplaceable role.

The ca. 660–630 Ma magmatic event is manifested by the following; (i) potassic granitoids (Ge et al., 2012) and mafic dykes (Zhu et al., 2008) in the Korla area, (ii) the presence of peraluminous granite at the Tarim-western Tianshan boundary and in the core of the Tugerming Anticline at the northern margin of Tarim Craton, and (iii) the occurrence of the basaltic and andesitic lavas in the central Quruqtagh (Xu et al., 2009). As discussed above, this magmatic event probably recorded the transition of a continental arc to a back-arc rift following an Early Pan-African retreating accretionary orogeny. This event was probably triggered by slab rollback and seaward migration of the subduction zone. It should be pointed out that the intensity and extent of this magmatic event are relatively limited, which might be attributed to the high-angle subduction and relatively narrow back-arc region after slab rollback. The uncertainties of this model lie in position and extent of continental arc during and after the accretionary event. One possibility is that it might lie in the Central Tianshan Block, which was detached from the northernmost Tarim during the early Paleozoic (Ge et al., 2012), or it had been eroded, reworked, or deeply buried.

6.2. Regional tectonic implications

A tectono-thermal event at 1.8–2.1 Ga was widespread on a global scale and may have resulted in the formation of the supercontinent Columbia (Rogers and Santosh, 2002, 2003; Michael, 2007; Long et al., 2011). The northern Tarim Craton contains abundant late Paleoproterozoic zircons contemporaneous with the assembly of the supercontinent Columbia (Zhang et al., 2007; Shu et al., 2011; Long et al., 2011, 2012). In contrast, in the eastern Tarim Craton, geological records related to the formation of the supercontinent Columbia are rarely reported. In the eastern Altyn Tagh-Dunhuang region, intrusions of 2.5–2.3 Ga trondhjemites (gneiss) and mafic dykes are widely exposed and interpreted as bimodal intrusive rocks, indicative of magmatism in a rift-related setting (Lu et al., 2008). In the eastern Altyn Tagh Mountains, a number of orthogneisses have been recognized. In addition, tonalite gneisses of 2604 ± 102 Ma and monzonitic gneisses of 2830 ± 45 Ma are also reported in that area (Lu and Yuan, 2003; Lu et al., 2008). In the Dunhuang Group, located in the eastern Tarim Craton, the age spectra of the detrital zircons from the three analyzed samples are mainly clustered at 2417 Ma, 2174 Ma and 1953 Ma (Wang et al., 2013). In our study, the zircon SIMS U–Pb dating of the Daxigou intrusion yielded weighted mean ages of 2452 ± 10 Ma, indicating that the Tarim Craton had widely experienced multiple tectono-thermal events during the Paleoproterozoic.

The Tarim Craton is a typical platform with Neoarchean to early Neoproterozoic basement unconformably overlain by middle Neoproterozoic to Cambrian unmetamorphosed cover (Lu et al., 2008; Zhang et al., 2012a, 2012b), which has been further subdivided into the Sinian and Nanhua Systems of which the former contains three sequences of tillite and the latter contains one sequence of tillite. Therefore, the middle Neoproterozoic cover of the Tarim Craton is a unique Neoproterozoic succession in the world that contains all four sequences of Neoproterozoic tillites that is considered as a hallmark of the Neoproterozoic snowball Earth (Hoffman and Schrag, 2000). In the Quruqtagh, the middle Neoproterozoic diamictite sequences are called the Quruqtagh Group, which overlies the late Mesoproterozoic to early Neoproterozoic Paergangtage Group and underlies the Cambrian Xishanblaq Formation that contains abundant basal Cambrian acritarchs and small shelly fossils. The Quruqtagh Group is subdivided, from bottom to top, into the Bayisi, Zhaobishan, Altungoul, Tereeken, Zhamoketi, Yukengou, Shuiquan, and Hankalchough formations, of which the Bayisi, Altungoul, Terrken and Hankalchough formations contain glacial diamictites, indicating at least three episodes of glaciation in the middle Neoproterozoic (Lu et al., 2008; Xu et al., 2009). Xu et al. (2009) obtained SHRIMP U-Pb zircon ages of 740 ± 7 Ma and 725 ± 10 Ma for volcanic rocks from the base and top successions of the Bayisi diamictite, respectively, and an age of 615 ± 6 Ma for a volcanic rock layer between the Tereeken and Hankalchough diamictites. Xu et al. (2009) and Lu et al. (2008) proposed that the development of the middle Neoproterozoic Kuruketage Group was coincident with the breakup of the Rodinia, which is consistent with the presence of the bimodal volcanic rocks in the Quruqtagh Group and the widespread emplacement of the middle to late Neoproterozoic ultramafic-mafic complexes and mafic dykes in the Tarim Craton (Lu et al., 2008). Zhang et al. (2012a, 2012b) recognized four phases of the middle-late Neoproterozoic igneous activities in the Quruqtagh, namely: (1) the ca. 820–800 Ma ultramafic-mafic-carbonatite complex and voluminous adakitic granites and mafic dyke swarm; (2) the ca. 780–760 Ma tholeiitic ultramafic-mafic complex and voluminous mafic dyke swarm; (3) the ca. 740–735 Ma bimodal complex and bimodal volcanic series; and (4) minor 650–635 Ma mafic dykes. The Neoproterozoic igneous activities waned since 740 Ma as a result of the dispersion of the Tarim from Rodinia. Zhang et al. (2012a, 2012b) argue that the emplacement of these middle and late Neoproterozoic igneous rocks was related to a mantle plume event that led to the breakup of the Tarim Craton from the Rodinia supercontinent (Zhang et al., 2012a, 2012b). The other Cu-Ni, Fe-P and apatite-vermiculite deposits hosted in the ultramafic–mafic-carbonatite rocks formed between 812 Ma and 707 Ma. Our preferred interpretation of these Neoproterozoic ultramafic-mafic-carbonatite is that they were related to a mantle plume event that led to the breakup of the Tarim Craton from the Rodinia supercontinent.

7. Conclusions

Conclusions from our SIMS U-Pb zircon ages and geochemical data for the Cu-Ni, Fe-P, and apatite-vermiculite deposits in the Quruqtagh domain can be summarized as follows; Most of the ultramafic–mafic-carbonatite rocks and Cu-Ni, Fe-P, and apatite-vermiculite deposits (e.g. the Xingdi, Qieganbulake, Kawuliuke deposits) in Quruqtagh formed in the Neoproterozoic (812–707 Ma), though minor deposits (e.g. Daxigou Fe-P deposit) may have formed in the Paleoproterozoic (at ~2452 ± 10 Ma). The Paleoproterozoic Fe-P mineralization was related to the assembly of the Paleo-Mesoproterozoic Columbia (Nuna) supercontinent. And the emplacement of these Neoproterozoic ultramafic–mafic-carbonatite rocks was related to a mantle plume event that led to the breakup of the Tarim Craton from the Rodinia supercontinent.

Conflict of interest

We declare that we have no financial and personal relationships with other people or organizations that can inappropriately influence our work, there is no professional or other personal interest of any nature or kind in any product, service and/or company that could be construed as influencing the position presented in, or the review of, the manuscript entitled.

Acknowledgements

We are indebted to Xianhua Li, Jingwen Mao, Bin Cui, Kezhang Qin, Lianchang Zhang, Tianlin Ma and Jianming Yang for their thoughtful discussions. Many of the ideas in this paper were initiated and rectified during these discussions. In particular, we thank Deru Xu, Zhaochong Zhang and Guochun Zhao for their perceptive comments, which led to

Please cite this article as: Han, C., et al., Ages and tectonic implications of the mafic–ultramafic-carbonatite intrusive rocks and associated Cu-Ni, Fe-P and apatite-vermic..., Ore Geol. Rev. (2016), http://dx.doi.org/10.1016/j.oregeorev.2016.07.011

substantial improvements to the paper. Two anonymous reviewers, and the Editor, Franco Pirajno, are thanked for their constructive reviews, which significantly improved the manuscript. This study was financially supported by funds from the Summary of the North China block iron ore deposits metallogenic regularity (20,089,950), the Strategic Priority Research Program (B) of the Chinese Academy of Sciences (XDB18020203), and the NSFC projects (41,230,207, 41,190,075, 41,390,441, 40,421,303, and 40,572,043). This paper is a contribution to IGCP 592

References

Brookfield, M.E., 1994. Problems in applying preservation facies and sequence models to Sinian (Neoproterozoic) glacial sequences in Australia and Asia. Precambrian Res. 70, 143–147.

Cao, X.F., Lv, X.B., Lei, J.H., Chen, C., Wang, Y.Q., Du, B.F., Mei, W., Gao, X., Du, A.D., 2010. The age of the Neoproterozoic Dapingliang skarn copper deposit in Kuruketage, NW China. Resource Geo. 60, 397–403.

Cao, X.F., Lv, X.B., Liu, S.T., Zhang, P., Gao, X., Chen, C., Mo, Y.L., 2011. LA-ICP-MS zircon dating, geochemistry, petrogenesis and tectonic implications of the Dapingliang Neoproterozoic granites at Kuluketage Block, NW China. Precambrian Res. 186, 205–219.

Chen, G.Y., 1989. Geologic features of the vermiculite deposit in Yuli and its genetic reasoning. Xinjiang Geol. 7, 1–14 (in Chinese with Englist abstract).

Deng, X.L., Shu, L.S., Zhu, W.B., 2008. Geochronology of the Precambrian structure magmatism-deformation along the Xindi fault in Xinjiang, NW China. Acta Petrol. Sin. 24, 2800–2808 (in Chinese with English abstract).

Feng, B.Z., Zhou, Y.W., Chi, S.F., Yang, T.Q., Zhong, C.X., Ye, S.Q., 1995. Pre-Sinian Geology and Noble Metals, Colored Metals Mineralization in Quruqtagh, Xinjiang. Geological Publishing House, Beijing, pp. 1–282 (in Chinese with English abstract).

Gao, Z., Qian, J., 1985. Sinian glacial deposits in Xinjiang, Northwest China. Precambrian Res. 29, 143–147.

Gao, Z., Zhu, C., 1984. Precambrian Geology in Xinjiang, China. Urumqi. pp. 1–151 (in Chinese with English abstract).

Gao, Z.J., Chen, J.B., Lu, S.N., Peng, C.W., Qin, Z.Y., 1993. The Precambrian geology in northern Xinjiang. Precambrian Geology No. 6. Geological Publishing House, Beijing (171 pp).

Gao, J., He, G., Li, M., Xiao, X., Tang, Y., Wang, J., Zhao, M., 1995. The mineralogy, petrology, metamorphic P-T-D-t trajectory and exhumation mechanism of blueschists, south Tianshan, northwest China. Tectonophysics 250, 151–168.

Gao, S., Liu, X.M., Yuan, H.L., Hattendorf, B., Gunther, D., Chen, L., Hu, S.H., 2002. Determination of forty two major and trace elements in USGS and NIST SRM glasses by laser ablation inductively coupled plasma-mass spectrometry. Geostand. Newslett. J. Geostand. Geoanal. 26, 191–196.

Ge, R.F., Zhu, W.B., Zheng, B.H., Wu, H.L., He, J.W., Zhu, X.Q., 2012. Early Pan-African magmatism in the Tarim Craton: insights from zircon U–Pb–Lu–Hf isotope and geochemistry of granitoids in the Korla area, NW China. Precambrian Res. 212–213, 117–138.

Gehrels, G.E., Yin, A., Wang, X., 2003. Magmatic history of the northeastern Tibetan plateau. J. Geophys. Res. 108, 2423. http://dx.doi.org/10.1029/2002JB001876.

Guo, Z.J., Yin, A., Robinson, A., Jia, C.Z., 2005. Geochronology and geochemistry of deepdrill-core samples from the basement of the central Tarim basin. J. Asian Earth Sci. 25, 45–56.

Hoffman, P.F., Schrag, D.P., 2000. Snowball Earth. Sci. Am. 282, 68–75.

Hu, A.Q., Jahn, B.M., Zhang, G.X., Chen, Y.B., Zhang, Q.F., 2000. Crustal evolution and Phanerozoic crustal growth in northern Xinjiang: Nd isotope evidence. 1. Isotopic characterization of basement rocks. Tectonophysics 328, 15–51.

Huang, J.H., 2001. Study on the Genesis of the Qieganbulake Superlarge Apatite-Vermiculite Deposits at Yuli County, Xinjiang, China Ph.D. Thesis Nanjing University, pp. 27–30 (in Chinese with Englist abstract).

Huang, J.H., Wu, C.Z., Lei, R.X., Chen, G., Xiong, L.M., Qin, Q., Gu, L.X., 2002. Genesis and ore-forming model of Qieganbulak superlarge vermiculite deposit in Xinjiang. Mineral Deposits 31, 359–368 (in Chinese with English abstract).

Huang, B.C., Xu, B., Zhang, C.X., Li, Y.A., Zhu, R.X., 2005. Paleomagnetism of the Baiyisi volcanic rocks (ca. 740 Ma) of Tarim, Northwest China: a continental fragment of Neoproterozoic Western Australia? Precambrian Res. 142, 83–92.

Jiang, C.Y., Lu, D.R., Bai, K.Y., Zhang, P.B., Ye, S.F., Feng, J.X., Chen, W.G., 2005. Metasomatism products of continental lithosphere mantle-roseite deposits, Qieganbulake. Acta Petrol. Sin. 21, 201–210.

Knoll, A.H., 2000. Learning to tell Neoproterozoic time. Precambrian Res. 100, 3–20.

Li, Z.X., Bogdanova, S.V., Collins, A.S., Davidson, A., De Waele, B., Ernst, R.E., Fitzsimons, I.C.W., Fuck, R.A., Gladkochub, D.P., Jacobs, J., Karlstrom, K.E., Lu, S., Natapov, L.M., Pease, V., Pisarevsky, S.A., Thrane, K., Vernikovsky, V., 2008. Assembly, configuration, and breakup history of Rodinia: a synthesis. Precambrian Res. 160, 179–210.

Li, X.H., Li, Z.X., Ge, W., Zhou, H., Li, W., Liu, Y., Wingate, M.T.D., 2003a. Neoproterozoic granitoids in South China: crustal melting above a mantle plume at ca. 825 Ma? Precambrian Res. 122, 45–83.

Li, Z.X., Li, X.H., Kinny, P.D., Wang, J., Zhang, S., Zhou, H., 2003b. Geochronology of neoproterozoic *syn*-rift magmatism in the Yangtze Craton, South China and correlations with other continents: evidence for amantle superplume that broke up Rodinia. Precambrian Res. 122, 85–109.

Li, Z.X., Li, X.H., Kinny, P.D., Wang, J., 1999. The breakup of Rodinia: did it start with a mantle plume beneath South China? Earth Planet. Sci. Lett. 173, 171–181.

Li, X.H., Liu, Y., Li, Q.L., Guo, C.H., Chamberlain, K.R., 2009a. Precise determination of Phanerozoic zircon Pb/Pb age by multi-collector SIMS without external standardization. Geochem. Geophys. Geosyst. 10, Q04010. http://dx.doi.org/10.1029/cGC002400.

Li, Q.L., Li, X.H., Liu, Y., Tang, G.Q., Yang, J.H., Zhu, W.G., 2009b. Precise U-Pb and Pb-Pb dating of phanerozoic zircon Pb/Pb age by multi-collector SIMS without external standardization. Geochem. Geophys. Geosyst. 10. http://dx.doi.org/10.1029/CGC002400.

Li, H.Q., Xie, C.F., Chang, H.L., Cai, H., Zhu, J.P., Zhou, S., 1998. Study on the Metallogenetic Chronology of Nonferrous and Precious Metallic Ore Deposits in North Xinjiang. Geological Publishing House, China, Beijing, pp. 1–250 (in Chinese with English abstract).

Long, X.P., Sun, M., Yuan, C., Kröner, A., Hu, A.Q., 2012. Zircon REE patterns and geochemical characteristics of Paleoproterozoic anatectic granite in the northern Tarim Craton, NW China: implications for the reconstruction of the Columbia supercontinent. Precambrian Res. http://dx.doi.org/10.1016/j.precamres.2011.09.009.

Long, X.P., Yuan, C., Sun, M., Kröner, A., Zhao, G.C., Wilde, S.A., Hu, A.Q., 2011. Reworking of the Tarim Craton by underplating of mantle plume-derived magmas: evidence from Neoproterozoic adakitic rocks and I-type granites in the Kuluketage area, NW China. Precambrian Res. 187, 1–14.

Lu, S.N., 2002. Preliminary Study of Precambrian Geology in the North Tibet-Qinghai Plateau. Geological Publishing House, Beijing, p. 125.

Lu, S.N., Yuan, G.B., 2003. Geochronology of early Precambrian magmatic activities in Aketasdhtage, east Altyn tagh. Acta Geol. Sin. 77, 61–68 (in Chinese with English abstract).

Lu, S.N., Li, H.K., Zhang, C.L., Niu, G.H., 2008. Geological and geochronological evidence for the Precambrian evolution of the Tarim craton and surrounding continental fragments. Precambrian Res. 160, 94–107.

Ludwig, K.R., 2001. Users manual for Isoplot/Ex rev. 2.49. Berkeley Geochronology Centre Special Publication, No. 1a (56 pp.).

Luo, J.H., Che, Z.C., Zhang, X.L., Han, W., Zhang, G.F., Nian, X.Q., 2011. Neoproterozoic granitoid magmatism in the Kuqe depression of Northeastern Tarim Basin and its significance. Acta. Geol. Sin. 85, 467–474 (in Chinese with English abstract).

Michael, B., 2007. Metamorphism, plate tectonics, and the supercontinent cycle. Earth Sci. Front. 14, 1–18.

Rogers, J.J.W., Santosh, M., 2002. Configuration of Columbia, a Mesoproterozoic supercontinent. Gondwana Res. 5, 5–22.

Rogers, J.J.W., Santosh, M., 2003. Supercontinents in earth history. Gondwana Res. 6, 357–368.

Shu, L.S., Deng, X.L., Zhu, W.B., Ma, D.S., Xiao, W.J., 2011. Precambrian tectonic evolution of the Tarim Block, NW China: new geochronological insights from the Quruqtagh domain. J. Asian Earth Sci. 42, 774–790.

Shu, L.S., Yu, J.H., Charvet, J., Laurent-Charvet, S., Zhang, R.G., Sang, H.Q., 2004. Geological, geochronological and geochemical features of granulites in the Eastern Tianshan, NW China. J. Asian Earth Sci. 24 (1), 25–41.

Stacey, J.S., Kramers, J.D., 1975. Approximation of terrestrial lead isotope evolution by a two-stage model. Earth Planet. Sci. Lett. 26, 207–221.

Sun, B.S., Huang, J.H., 2007. Sm-Nd isotopic age of Qieganbulak ultrabasic-carbonatite complex in Xinjiang, China and its geological significance. Acta Petrol. Sin. 23, 1611–1616 (in Chinese with English abstract).

Sun, S.S., McDonough, W.F., 1989. Chemical and isotopic systematics of oceanic basalts: implications for mantle composition and processes. Geol. Soc. Lond. Spec. Publ. 42, 313–345.

Wang, Z.M., Han, C.M., Su, B.X., Sakyi, P.A., Sanjeewa, P.K.M., Ao, S.J., Wang, L.J., 2013. The metasedimentary rocks from the eastern margin of the Tarim Craton: petrology, geochemistry, zircon U–Pb dating, Hf isotopes and tectonic implications. Lithos 179, 120–136.

Wang, Y., Lu, S., Gao, Z., Lin, W., Ma, G., 1981. Sinian tillites of China. In: Hambrey, M.J., Harland, W.B. (Eds.), Earth's Pre-Pleistocene Glacial Record. Cambridge, pp. 386–401.

Wiedenbeck, M., Alle, P., Corfu, F., Griffin, W.L., Meier, M., Oberli, F., Vonquadt, A., Roddick, J.C., Speigel, W., 1995. Three natural zircon standards for U–Th–Pb, Lu–Hf, trace element and REE analyses. Geostand. Newslett. 19, 1–23.

Windley, B.F., Alexeiev, D., Xiao, W.J., Kroner, A., Badarch, G., 2007. Tectonic models for accretion of the Central Asian Orogenic Belt. J. Geol. Soc. Lond. 164, 31–47.

Wu, F.Y., Yang, Y.H., Xie, L.W., Yang, J.H., Xu, P., 2006. Hf isotopic compositions of the standard zircons and baddeleyites used in U–Pb geochronology. Chem. Geol. 234, 105–126.

Xia, X.H., Tan, Y.J., Yang, H.Y., Yuan, J.Z., Luang, Z.P., Xi, G.Q., 2012. The feasibility study and metallogenic predicition of endogenssis phosphorite resources in the northern edge of Tarim platform. Geol. China 39, 486–496 (in Chinese with English abstract).

Xia, X.H., Xi, G.Q., Yuan, J.Z., Luang, Z.P., 2011. Study on geology and comprehensive utilization of magnetite and apatite deposit of Kawuliuketag in Xinjiang. Geol. Chem. Miner. 33, 191–200 (in Chinese with English abstract).

Xia, X.H., Yuan, J.Z., Xi, G.Q., Yan, F., Han, B., 2009. The feasibility study and metallogenic predicition of endogenssis phosphorite resources in the northern edge of Tarim platform. Geol. Chem. Miner. 31, 129–158 (in Chinese with English abstract).

Xiao, S.H., Bao, H.M., Wang, H.F., Kaufmand, A.J., Zhou, C.M., Li, G.X., Xunlai Yuan, X.L., Ling, H.F., 2004. The Neoproterozoic Quruqtagh Group in Eastern Chinese Tianshan: evidence for a post-Marinoan glaciation. Precambrian Res. 130, 1–26.

Xiao, W., Windley, B., Sun, S., Li, J., Huang, B., Han, C., Yuan, C., Sun, M., Chen, H., 2015. A tale of amalgamation of three collage systems in the Permian-Middle Triassic in Central Asia: oroclines, sutures and terminal accretion. Annu. Rev. Earth Planet. Sci. 43, 477–507. http://dx.doi.org/10.1146/annurev-earth-060614-105254.

Xinjiang BGMR, 1993. Regional Geology of the Xinjiang Uygur Autonomous Region. Geological Publishing House, Beijing, pp. 17–45 (in Chinese).

Xu, B., Kou, X.W., Song, B., Wei, W., Wang, Y., 2008. SHRIMP dating of the upper Proterozoic volcanic rocks in the Tarim plate and constraints on the Neoproterozoic glaciations. Acta Petrol. Sin. 24, 2857–2862 (in Chinese with English abstract).

Please cite this article as: Han, C., et al., Ages and tectonic implications of the mafic–ultramafic-carbonatite intrusive rocks and associated Cu-Ni, Fe-P and apatite-vermic..., Ore Geol. Rev. (2016), http://dx.doi.org/10.1016/j.oregeorev.2016.07.011

Xu, B., Jian, P., Zheng, H., Zou, H., Zhang, L., Liu, D., 2005. U–Pb zircon geochronology and geochemistry of Neoproterozoic volcanic rocks in the Tarim Block of northwest China: implications for the break-up of Rodinia supercontinent and Neoproterozoic glaciations. Precambrian Res. 136 (2), 107–123.

Xu, B., Xiao, S.H., Zou, H.B., Chen, Y., Li, Z.X., Song, B., Liu, D.Y., Zhou, C.M., Yuan, X.L., 2009. SHRIMP zircon U–Pb age constraints on Neoproterozoic Quruqtagh diamictites in NW China. Precambrian Res. 168, 247–258.

Xu, B., Zheng, H., Yao, H., Li, Y., 2003. C-isotope composition and significance of the Sinian on the Tarim plate. Chin. Sci. Bull. 48 (4), 385–389.

Ye, H.M., Li, X.H., Lan, Z.W., 2013. Geochemical and Sr–Nd–Hf–O–C isotopic constraints on the origin of the Neoproterozoic Qieganbulake ultramafic-carbonatite complex from the Tarim Block, Northwest China. Lithos 182-183, 150–164.

Yin, B.X., 1992. Discussion on genesis and pattern of the pelhamite deposit in Yuli, Xinjing. Xinjiang Geol. 10, 6–21 (in Chinese with Englist abstract).

Yuan, Y.X., Pan, Z.X., Qian, Y.Z., 2002. Cu–Ni bearing property evaluation of Xingdi complex no. 2 in Kuruktage, Xinjiang. Xinjiang Geol. 20, 49–52 (in Chinese with English abstract).

Zhang, C.L., Li, Z.X., Li, X.H., Ye, H.M., 2009a. Neoproterozoic mafic dyke swarm in north margin of the Tarim, NW China: age, geochemistry, petrogenesis and tectonic implications. J. Asian Earth Sci. 35, 167–179.

Zhang, Z.Y., Zhu, W.B., Shu, L.S., Su, J.B., Zheng, B.H., 2009b. Neoproterozoic ages of the Kuruketage diabase dyke swarm in Tarim, NW China, and its relationship to the breakup of Rodinia. Geol. Mag. 146, 150–154.

Zhang, C.L., 2010. Diverse Permian magmatism in the Trarim Blockm NW China: genetically lonked to the Tarim mantle plume? Lithos 119, 537–552.

Zhang, Z.C., Kang, J.L., Kusky, T., Santosh, M., Huang, H., Zhang, D.Y., Zhu, J., 2012b. Geochronology, geochemistry and petrogenesis of Neoproterozoic basalts from Sugetbrak, northwest Tarim block, China: implications for the onset of Rodinia supercontinent breakup. Precambrian Res. 220–221, 158–176.

Zhang, C.L., Li, X.H., Li, Z.X., Lu, S.N., Ye, H.M., Li, H.M., 2007. Neoproterozoic ultramafic-mafic-carbonatite complex and granitoids in Quruqtagh of northeastern Tarim Block, western China: geochronology, geochemistry and tectonic implications. Precambrian Res. 152, 149–169.

Zhang, C.L., Li, Z.X., Li, X.H., Ye, H.M., Wang, A.G., Guo, K.Y., 2006. Neoproterozoic bimodal intrusive complex in the southwestern Tarim Block, Northwest China: age, geochemistry, and implications for the rifting of Rodinia. Int. Geol. Rev. 48, 112–128. http://dx.doi.org/10.2747/0020-6814.48.2.112.

Zhang, C.L., Li, H.M., Santosh, L., Zhengxiang, Z., Haibo, W., Hongyan, Y., Haimin, 2012a. Precambrian evolution and cratonization of the Tarim Block, NW China: petrology, geochemistry, Nd-isotopes and U–Pb zircon geochronology from Archaean gabbro-TTG-potassic granite suite and Paleoproterozoic metamorphic belt. J. Asian Earth Sci. 47, 5–20.

Zhang, C.L., Yang, C., Shen, J., Zhao, Y., Wang, A.G., Dong, Y.G., Guo, K.Y., 2003. Zircon SHRIMP age of neoproterozoic gneissoid granites in the West Kunlun and its significance. Geol. Rev. 49, 239–244 (in Chinese with English abstract).

Zhang, C.L., Yang, D.S., Wang, H.Y., Takahashi, Y., Ye, H.M., 2011. Neoproteroxoic mafic-ultramafic layered intrusion in Quruqtagh of northeastern Tarim Block, NW China: two phases of mafic igneous activity with different. Gondwana Res. 19, 177–190.

Zhao, G.C., Peter, A.C., 2012. Precambrian geology of China. Precambrian Res. 222–223, 13–54.

Zhu, Z.X., 2007. The Geological Components and Tectonic Evolution of South Tianshan, Xinjiang Ph.D. Thesis Chinese Academy of Geological Sciences, Beijing, pp. 1–210.

Zhu, W.B., Zhang, Z.Y., Shu, L.S., Lu, H.F., Su, J.B., Yang, W., 2008. SHRIMP U-Pb zircon geochronology of Neoproterozoic Korla mafic dykes in the Northern Tarim Block, NW China: implications for the long lasting break-up process of Rodinia. J. Geol. Soc. Lond. 165, 887–890.

Please cite this article as: Han, C., et al., Ages and tectonic implications of the mafic–ultramafic-carbonatite intrusive rocks and associated Cu-Ni, Fe-P and apatite-vermic..., Ore Geol. Rev. (2016), http://dx.doi.org/10.1016/j.oregeorev.2016.07.011